12-1-2017

High-Pressure Granulite Facies Overprinting During the Exhumation of Eclogites in the Bangong-Nujiang Suture Zone, Central Tibet: Link to Flat-Slab Subduction

Xiu Zheng Zhang
Guangzhou Institute of Geochemistry Chinese Academy of Sciences

Qiang Wang
Guangzhou Institute of Geochemistry Chinese Academy of Sciences

Yong Sheng Dong
Jilin University

Chunfu Zhang
Fort Hays State University

Qing Yun Li
Peking University

See next page for additional authors

Recommended Citation

Zhang, X.-Z., Wang, Q., Dong, Y.-S., Zhang, C., Li, Q.-Y., Xia, X.-P., & Xu, W. (2017). High-Pressure Granulite Facies Overprinting During the Exhumation of Eclogites in the Bangong-Nujiang Suture Zone, Central Tibet: Link to Flat-Slab Subduction. Tectonics, 36(12), 2918–2935. https://doi.org/10.1002/2017TC004774

AGU PUBLICATIONS

Tectonics

RESEARCH ARTICLE
10.1002/2017TC004774

Key Points:
- HP-UHP eclogites from western segment of the Bangong-Nujiang suture zone, central Tibet
- Multistage retrograde metamorphism, phase equilibria, and SIMS zircon and rutile U-Pb ages
- Granulite facies overprinting during the exhumation of eclogites linked to flat-slab subduction

Supporting Information:
- Supporting Information S1

Correspondence to:
X.-Z. Zhang and Q. Wang,
zhangxz@gig.ac.cn;
wqiang@gig.ac.cn

Citation:
Zhang, X.-Z., Wang, Q., Dong, Y.-S., Zhang, C., Li, Q.-Y., Xia, X.-P., & Xu, W. (2017). High-pressure granulite facies overprinting during the exhumation of eclogites in the Bangong-Nujiang suture zone, central Tibet: Link to flat-slab subduction. *Tectonics*, *36*, 2918–2935. https://doi.org/10.1002/2017TC004774

Received 18 AUG 2017
Accepted 2 NOV 2017
Accepted article online 13 NOV 2017
Published online 11 DEC 2017

High-Pressure Granulite Facies Overprinting During the Exhumation of Eclogites in the Bangong-Nujiang Suture Zone, Central Tibet: Link to Flat-Slab Subduction

Xiu-Zheng Zhang[1], Qiang Wang[1,2,3], Yong-Sheng Dong[4], Chunfu Zhang[5], Qing-Yun Li[6], Xiao-Ping Xia[1], and Wang Xu[4]

[1]State Key Laboratory of Isotope Geochemistry, Guangzhou Institute of Geochemistry, Chinese Academy of Sciences, Guangzhou, China, [2]CAS Center for Excellence in Tibetan Plateau Earth Science, Beijing, China, [3]College of Earth Sciences, University of Chinese Academy of Sciences, Beijing, China, [4]College of Earth Science, Jilin University, Changchun, China, [5]Department of Geosciences, Fort Hays State University, Hays, KS, USA, [6]MOE Key Laboratory of Orogenic Belts and Crustal Evolution, School of Earth and Space Sciences, Peking University, Beijing, China

Abstract The geometric transformation of a descending plate, such as from steep to flat subduction in response to a change from normal to overthickened oceanic crust during subduction, is a common and important geological process at modern or fossil convergent margins. However, the links between this process and the metamorphic evolution of the exhumation of oceanic (ultra)high-pressure eclogites are poorly understood. Here we report detailed petrological, mineralogical, phase equilibria, and secondary ion mass spectrometry zircon and rutile U-Pb age data for the Dong Co eclogites at the western segment of the Bangong-Nujiang suture zone, central Tibet. Our data reveal that the Dong Co eclogites experienced peak eclogite-facies metamorphism (T = 610–630°C, P = 2.4–2.6 GPa) and underwent multiple stages of retrograde metamorphism. *P-T* pseudosections and compositional isopleths of garnet define a complex clockwise *P-T-t* path (including two stages of decompression-dominated *P-T* path and one of isobaric heating), suggesting varying exhumation velocities. Combining previous studies with our new results, we suggest that the transformation from rapid to slow exhumation is dominated by the transition from steep to flat subduction. The flat-slab segment, caused by subduction of buoyant oceanic plateau, led to an extremely slow exhumation and a strong overprinting of HP granulite facies at a depth of ~50 km at ~177 Ma. The slab rollback that followed in response to a substantial density increase of the eclogitized oceanic plateau resulted in another rapid exhumation process at ~168 Ma and triggered the formation of abundant near-simultaneous or later magmatic rocks.

1. Introduction

High-ultrahigh pressure (HP-UHP) rocks (e.g., eclogites) from worldwide metamorphic terranes provide robust evidence that the continental/oceanic crust can be dragged to more than 100 km depths and later be brought back to the Earth surface during the collision and/or convergent process (e.g., Agard et al., 2009; Chopin, 2003; Liou et al., 2004). Studies on the mechanisms, velocities, and dynamic processes for the exhumations of HP-UHP rocks can bring invaluable insights into plate tectonics and deep Earth processes (Agard et al., 2009; Cooper et al., 2011; Guillot et al., 2009; Hacker & Gerya, 2013; Kylander-Clark et al., 2009; Warren, 2013). Over the past 30 years, many studies focused on continental HP-UHP rocks (e.g., Burov et al., 2001; Ellis et al., 1999; Ernst, 2001), whereas oceanic eclogites received little attention. Different from the more buoyant continental crust, denser oceanic UHP eclogites are irreversibly buried, with only a few occasionally exhumed during specific time windows with the help of low-viscosity materials (e.g., serpentinite and sediment) after their decoupling from the subducting slab (e.g., Agard et al., 2009; Gerya et al., 2002).

Numerical modeling and geophysical studies suggest that the subduction of overthickened oceanic crust (aseismic ridges, oceanic plateaus, or seamount chains) could make the slab dip shallowly or even horizontally, resulting in a flat subduction (e.g., Gutscher, Spakman, et al., 2000; van Hunen et al., 2002). In fact, flat subduction occurs at about 10% of the world's convergent margins (Gutscher, Spakman, et al., 2000) and the alternation from steep to flat subduction should be a common geological process at modern or fossil convergent margins. Previous research reveals that flat subduction has broad implications for subduction zone

evolution, magmatism flare-up, continental crust growth, and intracontinental deformation (e.g., Bourdon et al., 2003; Gutscher, Spakman, et al., 2000; Gutscher, Maury, et al., 2000; Li & Li, 2007). To date, however, we know little about the relationship between flat-slab subduction and metamorphic evolution during the exhumation of oceanic eclogites.

The Dong Co eclogites were recently discovered in the Southern Qiangtang Block, Central Tibet (Dong et al., 2016), which made it possible to significantly improve our understanding of the Tethys Oceanic evolution during the Mesozoic Era. Previous studies revealed the existence of residual omphacites within the strongly retrogressed Dong Co eclogites (Dong et al., 2016) and suggested that their protolith could be a fragment of the Late Permian Bangong-Nujiang Tethys oceanic crust (Wang, Wang, Xu, et al., 2015; Zhang et al., 2015). However, so far, their refined *P-T* paths, metamorphic ages, exhumation mechanisms, and tectonic significance are still enigmatic. Here we report in detail the petrological features, mineralogical data, multi-stage retrograde metamorphism, phase equilibria, and secondary ion mass spectrometry (SIMS) zircon and rutile U-Pb ages for the Dong Co eclogites, which are then used to constrain the refined *P-T-t* paths and the metamorphic evolution history. Furthermore, our new results reveal a clear link between the HP granulite-facies overprinting during the exhumation of eclogites and flat-slab subduction.

2. Geological Setting and Field Occurrence

Tibet, located in Southwest China, is composed of several continental blocks (e.g., North Qiangtang, South Qiangtang, Lhasa, and Himalaya) (Figure 1a) that were progressively accreted to Asia as a result of the closure of the intervening Paleo-Tethyan and Neo-Tethyan oceans (Yin & Harrison, 2000; X. Z. Zhang et al., 2014). These continental blocks are separated by several significant suture zones, namely, the Jinsha (JSSZ), Longmu Co-Shuanghu (LSSZ), Bangong-Nujiang (BNSZ), and Yarlung Zangbo suture zones (IYZSZ) from north to south (Figure 1a). The BNSZ, extending east-west for $>$2,000 km in central Tibet, separates the South Qiangtang Block to the north and the Lhasa Block to the south (Figure 1b) (Yin & Harrison, 2000; Zhu et al., 2013). It is mainly composed of extensive dismembered ophiolitic fragments, Jurassic turbidites, minor retrograded eclogites, and high-pressure granulites (Figure 1b) (Dong et al., 2016; Wang, Wang, Chung, et al., 2015; Wang, Wang, Xu, et al., 2015; Zhang et al., 2010; Zhu et al., 2013, 2016). The ophiolites from the BNSZ, regarded as a crucial geological archive of the Bangong-Nujiang Tethyan oceanic lithosphere, were formed mainly during the Early to Middle Jurassic (190–164 Ma) according to U-Pb zircon dating (review from Wang, Wang, Chung, et al., 2015).

The eclogite samples from the Dong Co area are distributed in a ~1,500 m by ~400 m metamorphic belt (Figure 1c), occurring as blocks or lens-shaped bodies of sizes varying from a few meters to tens of meters in diameter, and are in contact with the surrounding metamorphic greywackes, ultramafic rocks, and schists (Figures 2a and 2b). The Dong Co eclogites were first reported as "HP granulite" (Wang, Wang, Xu, et al., 2015; Zhang et al., 2015) due to their strong overprinting at HP granulite facies to amphibolite-facies conditions. They were later identified as retrograded eclogites based on the discovery of minor residual omphacites (Dong et al., 2016). Here two omphacite-bearing samples (TC01-1 and TC01-4) were selected (Table 1) for detailed petrological, mineralogical, and phase equilibria studies. In addition, the sample TC01-1 was also selected for SIMS zircon and rutile U-Pb analyses. All analytical results are presented in the supporting information and Tables 2–4. A more detailed discussion of the methodology can be found in the supporting information (Bach et al., 1994, 1996; Bézos & Humler, 2005; Byerly, 1980; Coggon & Holland, 2002; Diener & Powell, 2012; Holland & Powell, 1998, 2003; Huang et al., 2007; Li et al., 2011, 2013, 2009; Liu et al., 2008; Ludwig, 2003; Powell et al., 1998; Puchelt & Emmermann, 1983; Sláma et al., 2008; White et al., 2000, 2002, 2007; Whitehouse et al., 1997; Zhao et al., 2011).

3. Results

3.1. Petrography

The eclogite samples (TC01-1 and TC01-4) in this study are mainly composed of garnet (20–30 vol %), clinopyroxene (15–25 vol %), plagioclase (20–30 vol %), amphibole (20–40 vol %), quartz ($<$5 vol %), and minor or accessory minerals (e.g., rutile, titanite, ilmenite, and apatite) (Figure 2c). The residual omphacites occur as rare minerals with sizes of 2–20 μm and were found within the clinopyroxene + sodic plagioclase symplectic intergrowths (Figures 2d and 2e). Two basic types of garnets have also been identified in the Dong Co

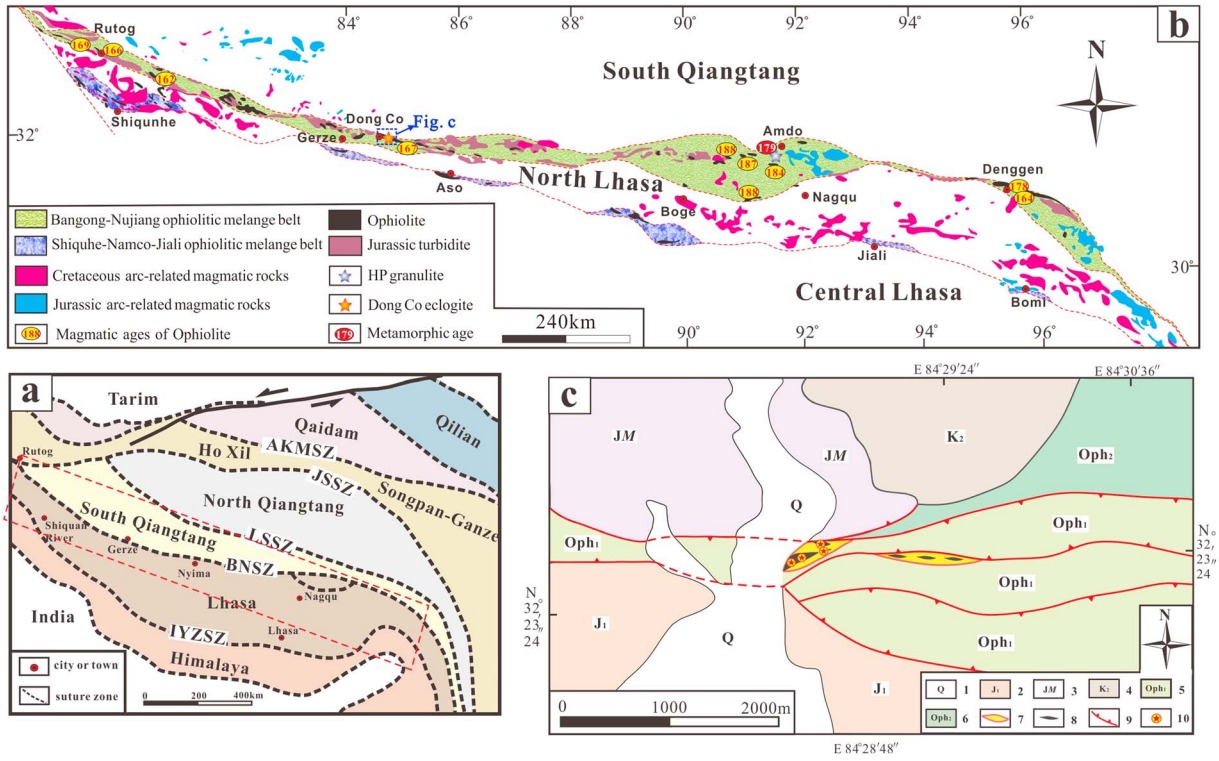

Figure 1. (a) Sketch map of Tibet (modified after X. Z. Zhang et al., 2014), showing the distribution of the main suture zones. JSSZ = Jinsha Suture Zone; LSSZ = Longmu Co-Shuanghu Suture Zone; BNSZ = Bangong-Nujiang suture zone; IYZSZ = Indus-Yarlung Zangbo Suture Zone. (b) Geologic map of the Bangong-Nujiang Suture Zone (modified after Wang, Wang, Chung, et al., 2015), showing the distribution of the ophiolites, arc-related magmatic rocks, and HP metamorphic rocks; (c) geologic map of the Dong Co area (modified after Zhang et al., 2015), showing the outcrops of eclogites and sample locations; 1—Quaternary deposits; 2—Upper Jurassic marine rocks; 3—Jurassic turbidites (Muggargangri Group); 4—Lower Cretaceous shallow marine clastic rocks; 5-ultramafic rocks of Jurassic ophiolites from BNSZ; 6—gabbros of Jurassic ophiolites from BNSZ; 7—metamorphic greywackes and schists; 8—eclogites; 9—thrust faults; 10—sample locations.

eclogites (TC01-1 and TC01-4): the small (<0.6 mm) Ca-rich irregular garnet (Grt_A, Type-A garnet) and large (1–3 mm) Mg-rich garnet porphyroblasts (Grt_B, Type-B garnet) (Figures 2c–2h), which is similar to many other granulitized eclogites in the world (e.g., granulitized eclogites from North Dabie Complex, Groppo et al., 2015). In addition, some clinopyroxenes (along with plagioclase and small Grt_A grains) occur as small inclusions in Grt_B porphyroblasts (Figures 2g and 2h), and amphibole + plagioclase ± ilmenite symplectites and coronas occur around these Grt_B grains (Figure 2h). The transitional reactions from rutile to ilmenite and titanite have also been observed in some thin sections (Figure 2i). Based on these reaction textures, the mineral assemblages in five different metamorphic stages (denoted with subscripts 1–5) are summarized in Table 1, including (1) a relic of eclogite facies assemblage (M_1); (2) clinopyroxene (augite) + sodic plagioclase (An < 30) symplectites (M_2, early decompression during posteclogite facies); (3) high-pressure granulite facies assemblage (M_3); (4) amphibole + plagioclase ± ilmenite symplectites (M_4, late decompression during post-HP granulite facies); and (5) amphibolite facies metamorphic assemblage (M_5).

3.1.1. Relic of Eclogite Facies Assemblage (M_1)

Due to the strong overprinting at subsequent granulite-facies conditions, much of the mineral and textural information concerning the early eclogite facies metamorphic history has been lost. The preserved eclogite facies assemblage has been recognized in only two samples (TC01-1 and TC01-4). They are represented by micron-sized omphacite (Omp_1) + core and mantle of Grt_A grains (Grt_1) within the symplectites of clinopyroxene (Cpx_2) + sodic plagioclase (Pl_2).

3.1.2. Clinopyroxene + Sodic Plagioclase Symplectites (M_2)

The postpeak eclogite facies assemblage in most retrograded eclogite samples investigated here mainly consists of Cpx_2 (augite) + sodic Pl_2 symplectites and coronas which developed around the eclogite facies minerals (Omp_1 + Grt_1). In the symplectic texture, Cpx_2 and Pl_2 occur as fine-grained, worm-like mineral

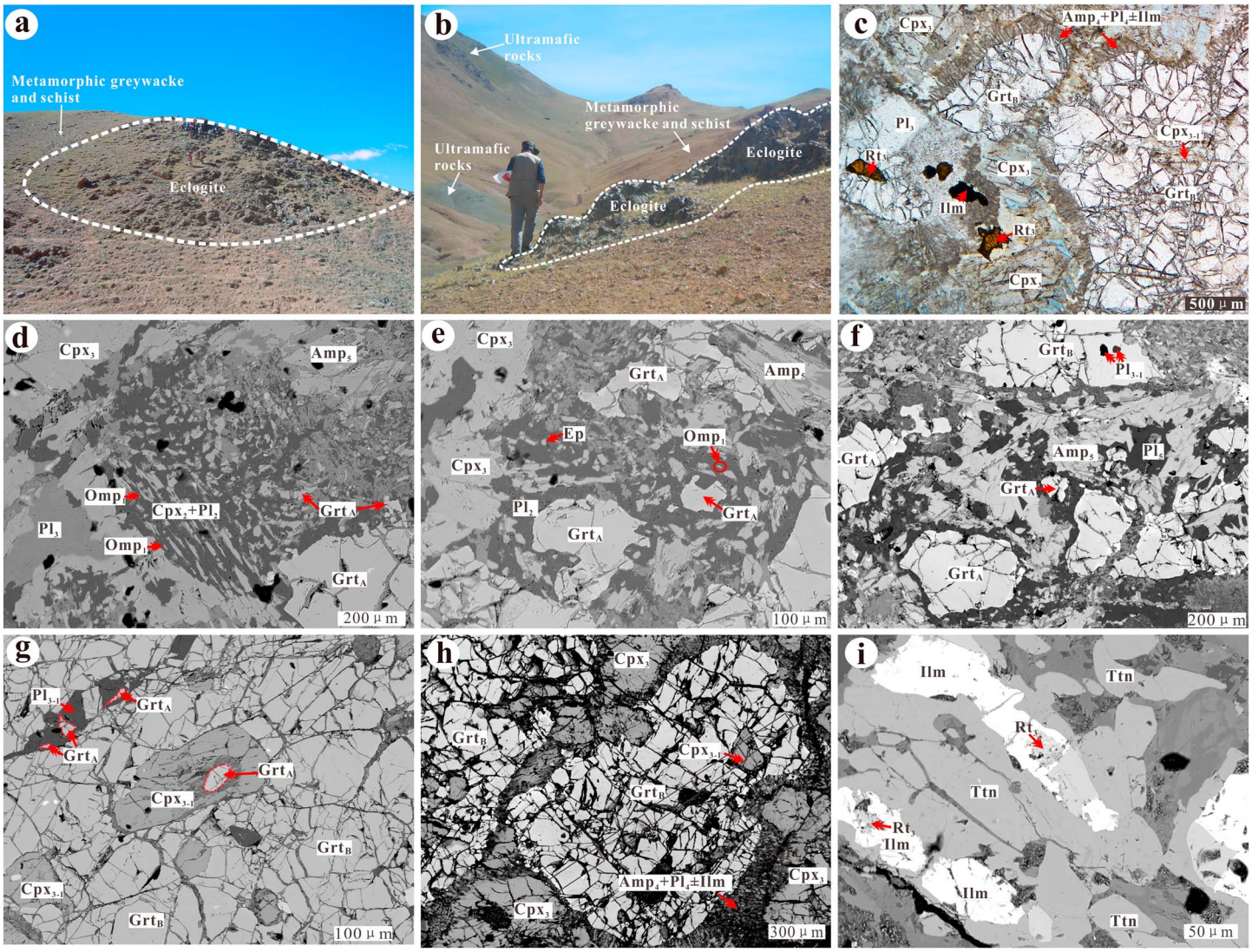

Figure 2. Field photographs, photomicrographs (plane polarized light), and backscattered electron (BSE) images of the Dong o eclogites from the Bangong-Nujiang Suture Zone, Tibet. (a and b) The Dong Co eclogites occur as blocks or lens-shaped bodies in contact with the surrounding metamorphic greywackes, ultramafic rocks, and schists; (c) most of the Dong Co eclogite samples are dominated by coarse-grained clinopyroxene, plagioclase, quartz, rutile, and large-sized garnet porphyroblasts in the matrix, indicating a strong overprinting at HP granulite facies conditions; (d) minor micron-sized omphacites within the Cpx_2 + sodic Pl_2 (An < 30) symplectic intergrowths; (e and f) irregular Grt_A (Ca-rich irregular Type-A garnet) occur as small-sized (<0.6 mm) remnants of early metamorphic minerals and are surrounded by Cpx_2 + Pl_2 symplectites or sodic Pl_2 coronas; (g) the mantle domains of large Grt_B (Mg-rich Type-B garnet porphyroblasts) generally contain small inclusions of clinopyroxene, plagioclase, sodic plagioclase (An < 30), and even early irregular garnets. (h) Amphibole + plagioclase ± ilmenite symplectites and coronas are present around Grt_B; and (i) the transformation from rutile, via ilmenite, to titanite in some thin sections.

intergrowths which are widely accepted as the breakdown products of jadeite-rich clinopyroxenes through the following solid-solid reaction (R_1) during the rapid decompression process after peak eclogite facies metamorphism (e.g., Möller, 1998; Zhao et al., 2001):

(R1) $$Omp_1 + Qtz_1 \rightarrow Sodic\ Pl_2 + Cpx_2$$

3.1.3. High-Pressure Granulite Facies Assemblage (M_3)

High-pressure granulites are generally accepted as containing distinct mineral assemblages of garnet + clinopyroxene + plagioclase + quartz, which are distinguished from eclogites by the existence of plagioclase and from medium pressure granulites by the lack of orthopyroxene (O'Brien & Rötzler, 2003; Zhao et al., 2001). The retrograded eclogite samples investigated in this study are dominated by coarse-grained clinopyroxene (diopside, Cpx_3), plagioclase (Pl_3), quartz (Qtz_3), and core and mantle of Grt_B porphyroblasts (Grt_3) in the

Table 1
Mineral Assemblages and Whole-Rock Compositions of the Dong Co Eclogites

Sample	TC01-1	TC01-4
Mineral assemblage	Grt, Omp, Cpx, Pl, Rt, Qtz, Amp, Ep, Czo, Zo, Ttn, Ilm, Zr	Grt, Omp, Cpx, Pl, Rt, Qtz, Amp, Ep, Zo, Ttn, Ilm, Zr, Mag
Metamorphic Stages		
M_1: ECL	$Omp_1 + Grt_1$	$Omp_1 + Grt_1$
M_2: ECL-HG	$Cpx_2 + Pl_2$	$Cpx_2 + Pl_2$
M_3: HG	$Grt_3 + Cpx_3 + Pl_3 + Rt_3 + Qtz$	$Grt_3 + Cpx_3 + Pl_3 + Rt_3 \pm Qtz$
M_4: HG-AM	$Cpx_4 + Pl_4 + Amp_4 \pm Ilm$	$Cpx_4 + Pl_4 + Amp_4 + Ilm \pm Mag$
M_5: AM	$Amp_5 + Pl_5 + Ttn_5 + Zo_5 \pm Qtz$	$Amp_5 + Pl_5 + Zo_5 + Ttn_5$
Whole-rock composition (mol %)	SiO_2 = 50.67, Al_2O_3 = 9.08, CaO = 14.23, MgO = 13.93, FeO = 8.53, K_2O = 0.05, Na_2O = 2.29, TiO_2 = 0.62, O = 0.58	SiO_2 = 49.58, Al_2O_3 = 9.76, CaO = 14.27, MgO = 13.91, FeO = 8.72, K_2O = 0.16, Na_2O = 2.10, TiO_2 = 0.91, O = 0.60

Note. Grt: garnet, Omp: omphacite, Cpx: clinopyroxene, Amp: amphibole, Pl: plagioclase, Qtz: quartz, Ep: epidote, Czo: clinozoisite, Zo: zoisite, Ttn: titanite, Ilm: ilmenite, Zr: zircon, Mag: magnetite. All mineral abbreviations are from Whitney and Evans (2010). Subscript numbers denote the metamorphic stages (M_1-M_5); ECL: eclogite facies; ECL-HG: early decompression during post-eclogite facies; HG: high-pressure granulite facies; HG-AM: late decompression during post-HP granulite facies; AM: amphibolite facies.

matrix, which are consistent with the observations of previous works (Wang, Wang, Xu, et al., 2015; Zhang et al., 2015). In addition, rutile is generally coexisting with the mineral assemblage of HP granulite facies in the matrix (Figure 2c) rather than that of eclogite facies as a residual symplectic mineral, thus indicating their formation at the HP granulite metamorphic stage ($Cpx_3 + Pl_3 + Grt_3 + Rt_3 \pm Qtz$). In some samples, characteristic HP granulite mineral assemblages are found as small inclusions (e.g., clinopyroxene and plagioclase, $Cpx_{3\text{-}I} + Pl_{3\text{-}I}$) in the mantle of Grt_3, which is similar to the Silurian high-pressure granulites from Central Qiangtang (X. Z. Zhang et al., 2014). In summary, the retrograded eclogites are dominated by characteristic HP granulite mineral assemblages, which indicates a strong overprinting at HP granulite facies conditions following the early eclogite facies.

3.1.4. Amphibole + Plagioclase ± Ilmenite ± Magnetite Symplectites (M_4)

Symplectic textures, consisting of intergrowths of a well-developed radial texture of amphibole (pargasite-edenite, Amp_4) + Ca-rich plagioclase (Pl_4) ± ilmenite ± magnetite around Grt_B porphyroblasts, are widespread in the retrograded eclogite samples investigated here. These symplectic textures have been observed in many granulite terranes and are generally regarded as an indicator of near-isothermal decompression experienced by the rocks after high-pressure granulite facies metamorphism (Harley, 1989; O'Brien & Rötzler, 2003; Zhao et al., 2001). The typical metamorphic reactions between the mineral phases at the M_4 stage are as follows (Harley, 1989; Zhao et al., 2001):

Table 2
In Situ Zircon SIMS U-Pb Dating Results for the Dong Co Eclogites (TC01-1)

Spot #	U (ppm)	Th (ppm)	Th U	f_{206}[a] (%)	$^{207}Pb/^{206}Pb$	±1σ (%)	$^{207}Pb/^{235}U$	±1σ (%)	$^{206}Pb/^{238}U$	±1σ (%)	$t_{207/235}$ (Ma)	±1σ	$t_{206/238}$ (Ma)	±1σ
1	55	44	0.79	0.11	0.0529	2.59	0.280	3.06	0.0383	1.62	250.5	6.8	242.6	3.9
2	23	18	0.76	0.23	0.0554	4.72	0.306	5.01	0.0401	1.69	270.9	12.0	253.2	4.2
3	248	227	0.92	0.16	0.0512	1.18	0.275	1.97	0.0390	1.57	246.8	4.3	246.4	3.8
4	381	642	1.69	0.13	0.0509	1.11	0.280	1.87	0.0398	1.50	250.4	4.2	251.7	3.7
5	25	16	0.63	0.63	0.0505	5.30	0.285	5.52	0.0410	1.53	254.8	12.5	259.0	3.9
6	40	25	0.64	0.11	0.0536	2.59	0.298	3.21	0.0403	1.89	264.6	7.5	254.4	4.7
7	63	51	0.81	0.19	0.0499	2.21	0.269	2.67	0.0391	1.50	241.7	5.8	246.9	3.6
8	484	464	0.96	0.09	0.0512	1.02	0.274	2.05	0.0388	1.78	245.9	4.5	245.6	4.3
9	265	258	0.97	55	0.0650	101	0.344	101	0.0383	2.67	299.9	234.1	242.4	6.4
10	664	760	1.14	0.05	0.0509	0.62	0.285	1.68	0.0407	1.56	254.9	3.8	257.0	3.9
11	479	479	1.00	0.08	0.0502	0.76	0.263	1.86	0.0380	1.70	237.3	3.9	240.5	4.0
12	450	405	0.90	0.24	0.0503	2.03	0.271	5.70	0.0392	5.32	243.9	12.4	247.6	12.9
13	41	30	0.73	0.13	0.0522	2.65	0.293	3.04	0.0407	1.50	260.8	7.0	257.4	3.8
14	399	410	1.03	0.02	0.0509	0.79	0.283	1.72	0.0403	1.53	253.0	3.9	254.7	3.8
15	1156	941	0.81	0.11	0.0500	0.89	0.188	1.84	0.0278	1.57	175.3	3.0	176.9	2.7

[a] f_{206} is the proportion of common ^{206}Pb in total measured ^{206}Pb.

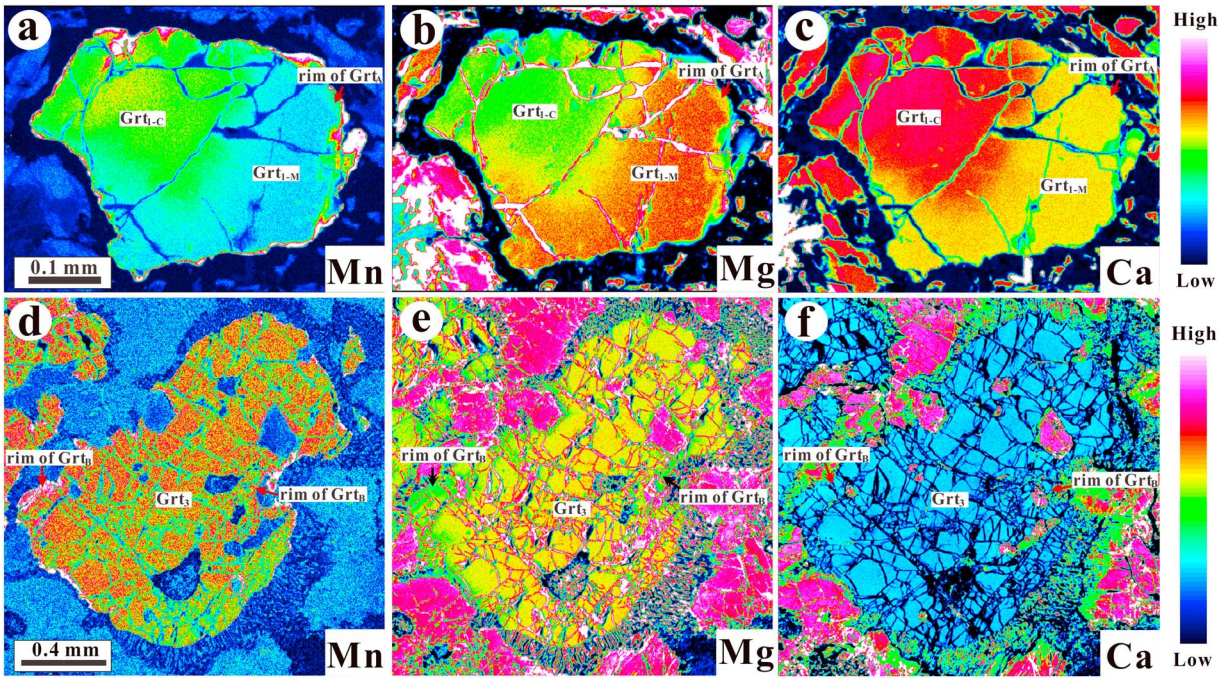

Figure 3. Element X-ray maps of (a - c) Grt_A and (d–f) Grt_B showing the five-stage growths or modifications.

(R2) $$Grt_3 + Cpx_3 + Qtz_3 + H_2O \pm O_2 \rightarrow Pl_4 + Amp_4 \pm Mt_4$$

(R3) $$Grt_3 + Rt_3 \rightarrow Ilm_4 + Pl_4 + Qtz_4$$

(R4) $$Grt_3 + Cpx_3 + H_2O \rightarrow Amp_4 + Pl_4$$

(R5) $$Grt_3 + Cpx_3 + Qtz_3 + H_2O \rightarrow Amp_4 + Pl_4$$

3.1.5. Amphibolite Facies Metamorphic Assemblage (M_5)

The late amphibolite-facies retrogression stage is represented by the amphibole (Amp_5) + plagioclase (Pl_5) assemblage. In most cases, matrix amphiboles (Amp_5) are developed at the expense of matrix clinopyroxene (Cpx_3) from the M_3 stage, thus confirming their status as the youngest metamorphic indicator minerals. The formation of amphibolite-facies metamorphic assemblage may be related to the following reaction (Harley, 1989):

(R6) $$Cpx_3 + Pl_3 + H_2O \rightarrow Amp_5$$

3.2. Mineral Major Elements

3.2.1. Garnet

Using elemental X-ray maps (Figure 3) and compositional profiles (Figure 4), the two basic types of garnets (Grt_A and Grt_B) can be subdivided into at least five stages, including core of Grt_A (Grt_{1-C}), mantle of Grt_A (Grt_{1-M}), outermost rim of Grt_A (diffusional re-equilibration of Grt_1 during early decompression process, M_1 to M_2), core and mantle of Grt_B (Grt_3), and outermost rim of Grt_B (diffusional re-equilibration of Grt_3 during late decompression process, M_3 to M_4). These five stages of garnets have varying compositions and were probably formed and/or modified at different metamorphic stages (Figures 4 and 5a).

A representative Grt_A from the sample TC01-1, which has a complete core-mantle-rim structure, is shown in Figures 3a–3c. The Grt_{1-C} is characterized by the highest contents of grossular (30–34 mol %) and spessartine (3–5 mol %), and by the lowest pyrope content (19–24 mol %) and $Mg^{\#}$ value [=100 × Mg/(Fe^{2+} + Mg)] (30–36). The Grt_{1-M} is characterized by moderate pyrope (24–30 mol %) and grossular (24–30 mol %) contents, higher $Mg^{\#}$ (35–40), and lower spessartine (2–3 mol %) (Figure 4a). The X-ray maps and a compositional profile reveal an increase in both pyrope content and $Mg^{\#}$ and a decrease in grossular and spessartine from Grt_{1-C} to Grt_{1-M} (Figures 3a–3c and 4a). The outermost rims of Grt_A are in contact with Cpx_2 + Pl_2 symplectite (M_2) and have probably been modified by diffusion and/or later metamorphic reactions. From mantle to

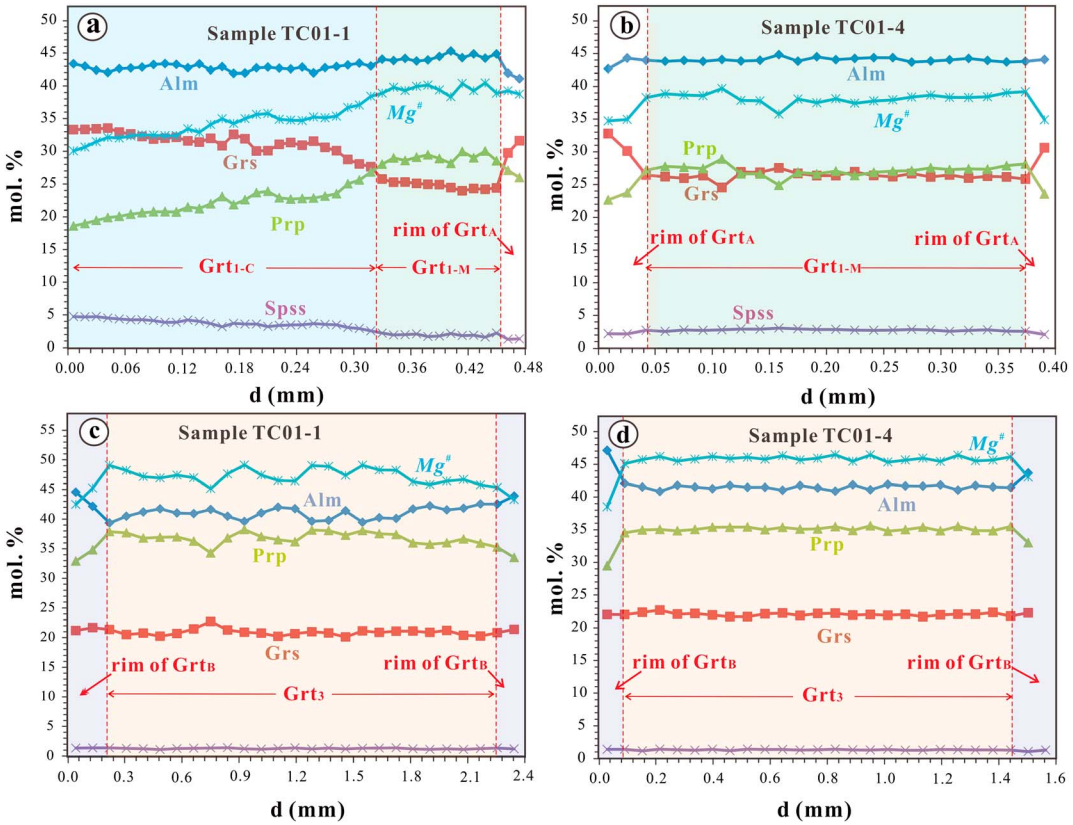

Figure 4. Compositional profiles of Grt_A and Grt_B from samples TC01-1 and TC01-4, showing the five-stage growths or modifications.

outermost rim of Grt_A, the pyrope content decreases while grossular content increases distinctly (Figures 4a and 4b). However, an irregular relict garnet with a complete core-mantle-rim structure is very rare and is only found in the sample TC01-1. In most cases (e.g., sample TC01-4), these irregular relict garnets only retain one or two generational fragments of mineral information during its growth (most of them have compositions similar to mantle and rim of Grt_A) (Figure 4b).

The Grt_3 grains consist mainly of pyrope (35–38 mol %), almandine (39–43 mol %), and grossular (20–23 mol %), with minor spessartine (~1 mol %) (Figures 4c, 4d, and 5a). They are distinguished from Grt_A by their homogeneous composition (Figures 3d–3f), lower spessartine content, and higher pyrope content and $Mg^{\#}$ value (45–49). By comparison, the outermost rims of Grt_B are in contact with symplectites or coronas of $Amp_4 + Pl_4 \pm Ilm_4 \pm Mag_4$ (M_4) and have lower pyrope (29–35 mol %) content and $Mg^{\#}$ (38–45) value (Figures 4c and 4d).

3.2.2. Clinopyroxene

The representative clinopyroxenes (Omp_1, Cpx_2, and $Cpx_3/Cpx_{3\text{-}I}$) of different stages from the Dong Co eclogites have been analyzed and the results are listed in Table S2. The residual Omp_1 grains contain 3.26–5.29 wt % Na_2O and significant amounts of the jadeite (Jd, 23–36 mol %) component and are plotted in the typical omphacite field (Figure 5b). Meanwhile, it is worth noting that they are also distinguished by the appearance of Ca-Eskola ($Ca_{0.5}\square_{0.5}AlSi_2O_6$, where $\square$ is a vacancy at the M_2 site) (1–23 mol %) (Table S2), which is very similar to the typical supersilicic omphacites from the eclogite xenoliths in kimberlites (Smyth, 1980) and the diamond-bearing UHP rocks in the Kokchetav massif (Katayama et al., 2000), suggesting the possibility of UHP metamorphism. Compared to the residual Omps, Cpx_2 (augite) grains from symplectites contain lower jadeite (Jd = 2–17 mol %) and have negligible Ca-Eskola component (0–2 mol %) (Figure 5c). In contrast, the Cpx_3 and $Cpx_{3\text{-}I}$ (diopside) grains contain the highest CaO (20.06–23.58 wt %) but the lowest Al_2O_3 (4.71–8.13 wt %) contents, with minor jadeite (3–7 mol %) (Figure 5c and Table S2).

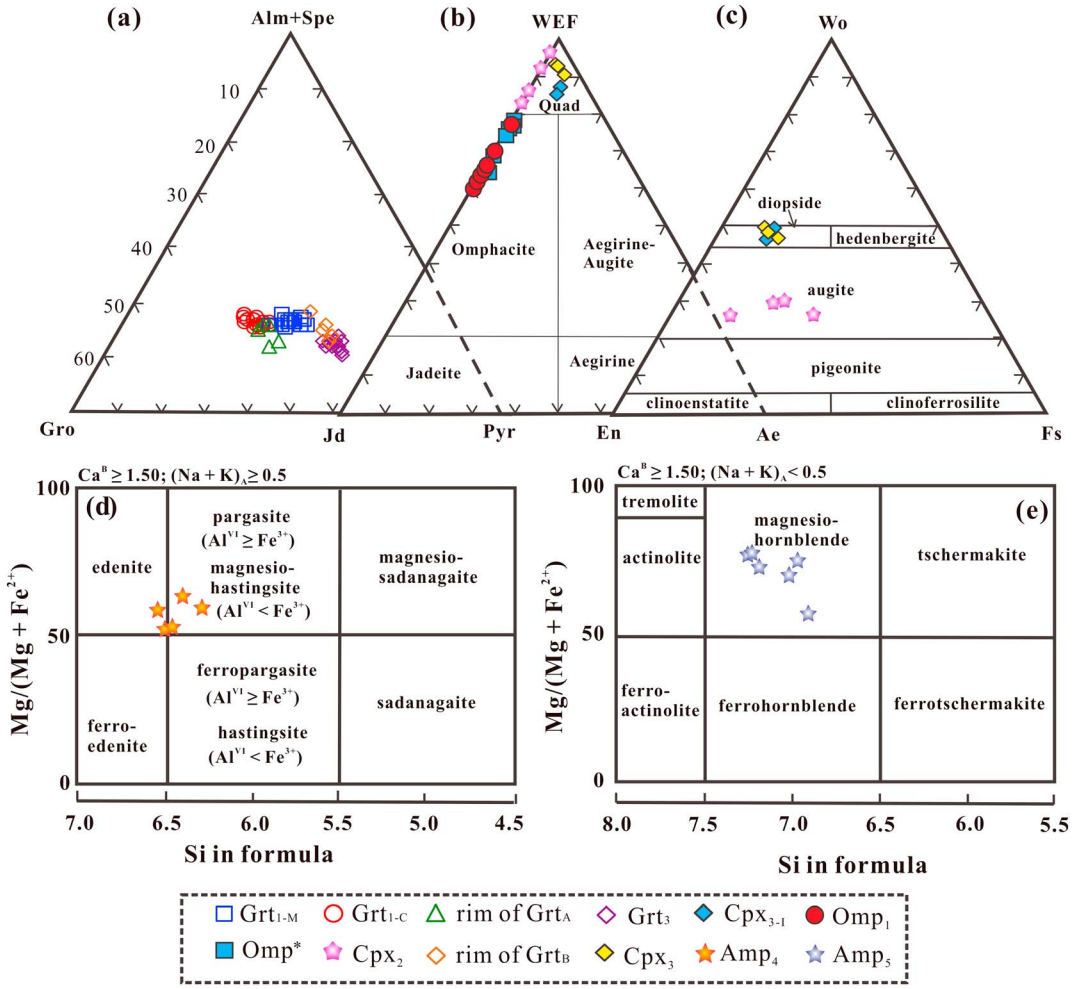

Figure 5. Chemical compositions of garnets, omphacites, and amphiboles in the Dong Co eclogites. (a) Composition of garnets from the Dong Co eclogites. Alm = almandine, Spe = spessartine, Gro = grossular, Pyr = pyrope. (b and c) Ternary classification diagram for sodic and Ca-Mg-Fe clinopyroxenes (after Morimoto et al., 1988), WEF = wollastonite + enstatite + ferrosilite, Jd = jadeite, Ae = aegirine, Wo = wollastonite, En = enstatite, Fs = ferrosilite. (d and e) Chemical classification diagram for amphiboles (after Leake et al., 1997).

3.2.3. Plagioclase

Representative plagioclase analyses, which are given in Table S3, include symplectic Pl_2 and Pl_4, matrix-type Pl_3 and Pl_5, and inclusion plagioclases ($Pl_{3\text{-}I}$). One remarkable feature of symplectic plagioclase is that the Pl_2 has the highest Ab (mol %) content (77–93), while the Pl_4 exhibits the highest An (mol %) content (68–85) (Table S3). Such differences suggest that the compositions of Pl_2 and Pl_4 are largely dependent on the breakdowns of omphacite (jadeite component, Na-rich) and garnet (grossular component, Ca-rich), respectively. Moreover, the Pl_3 and $Pl_{3\text{-}I}$ plagioclases from the HP granulite facies have moderate An component (45–52), which are slightly lower than those formed in the amphibolite facies (Pl_5) metamorphic stage (An = 57–64).

3.2.4. Amphibole

All the amphiboles in the Dong Co eclogites were formed during late retrograde metamorphism, including symplectic amphibole (Amp_4) and matrix-type Amp_5. Based on the nomenclature of Leake et al. (1997), the Amp_4 are pargasite to edenite (Figure 5d), with T_{Si} = 6.30–6.55, $(Na + K)_A > 0.5$, $Ti < 0.5$, $Al^{VI} > Fe^{3+}$, and $Mg^{\#}$ = 51–64. In contrast, all the Amp_5 are magnesiohornblende (Figure 5e) and are distinguished by T_{Si} = 6.90–7.25, $(Na + K)_A < 0.5$, and $Mg^{\#}$ = 70–77 (Table S4).

3.2.5. Other Minerals

Epidote-group minerals in the Dong Co eclogites include epidote, clinozoisite, and zoisite. Epidote and clinozoisite occur as small inclusions in mantle or rim of Grt_A and contain high FeO^T (5.26–8.72 wt %) but

Table 3
In Situ Rutile SIMS U-Pb Dating Results for the Dong Co Eclogites (TC01-1)

Spot	U (ppm)	f_{206}[a] (%)	$^{238}U/^{206}Pb$	±6 (%)	$^{207}Pb/^{206}Pb$	±6 (%)	$T_{206/238}$[b] (Ma)	±6 (%) (Ma)
TC01-01	1.6	6	35.7	5.9	0.099	16	167	10
TC01-02	1.6	2	33.3	5.0	0.075	8.5	185	9
TC01-03	2.5	3	36.5	4.1	0.070	8.2	170	7
TC01-04	3.3	2	34.9	9.3	0.061	9.2	180	17
TC01-05	3.8	2	35.4	6.5	0.057	8.7	178	12
TC01-06	2.8	3	37.5	4.5	0.071	10	165	8
TC01-07	2.2	3	36.8	7.3	0.062	12	170	12
TC01-08	3.9	1	38.6	7.3	0.065	9.9	162	12
TC01-09	5.3	1	37.6	3.7	0.061	7.2	167	6
TC01-10	2.9	2	37.6	4.0	0.063	4.1	166	7
TC01-11	2.9	2	37.9	5.3	0.065	11	164	9
TC01-12	5.2	1	36.4	5.0	0.054	3.4	174	9
TC01-13	2.5	2	39.4	7.2	0.075	5.1	156	11
TC01-14	1.8	10	31.8	6.1	0.130	11	179	12
TC01-15	1.4	3	38.4	4.2	0.085	16	158	7
TC01-16	1.1	5	37.8	8.4	0.109	9.3	156	13
TC01-17	4.9	1	38.3	3.6	0.052	7.4	165	6
TC01-18	2.1	24	29.7	6.8	0.237	9.2	163	13
TC01-19	4.3	1	39.6	5.0	0.063	2.0	158	8

[a]The percentage of common ^{206}Pb in total ^{206}Pb, calculated by ^{207}Pb-based. [b]The $^{206}Pb/^{238}U$ age calculated by ^{207}Pb-based common-lead correction.

low Al_2O_3 (26.55–28.30 wt %). Zoisite, by contrast, occurs as small grains in the matrix (usually in equilibrium with Amp_5) and is characterized by very high Al_2O_3 (31.71–31.84 wt %).

In addition, representative rutile, ilmenite, and titanite have also been analyzed and the data are given in Table S5.

3.3. SIMS Zircon and Rutile U-Pb Dating

A representative eclogite sample (TC01-1) was selected for SIMS zircon and rutile U-Pb analyses (Tables 2 and 3). Averaging 120–200 μm in length, the zircon grains are euhedral to subhedral, short prismatic to irregular in crystal shape, colorless, and mostly of magmatic origin with a broadly spaced zoning texture in cathodoluminescence (CL) images (Figure 6a). Some magmatic zircons, however, are surrounded by narrow (5–20 μm) moderate- to high-luminescence metamorphic rims (Figure 6a). The magmatic zircon grains yield a similar weighted mean age of 250.7 ± 3.7 Ma (MSWD = 2.3). One analysis from the metamorphic rim of a zircon grain yields a $^{206}Pb/^{238}U$ age of 176.9 ± 2.7 Ma (Figure 6b).

The rutile grains analyzed in this study range from 120 to 420 μm in length (Figure 6c) and exhibit uranium contents varying from 1.1 to 5.3 ppm (Table 3). Regression of the data points on the Tera-Wasserburg plot gives a lower intercept age of 167.6 ± 4.7 Ma (MSWD = 0.75, n = 19), which is consistent with the weighted mean $^{206}Pb^*/^{238}U^*$ age (^{207}Pb-based common-lead correction age, Williams, 1998) of 166.7 ± 3.9 Ma (MSWD = 0.67, n = 19) within errors (Table 3 and Figure 6d).

4. Discussion

4.1. *P-T* Estimates for Dong Co Eclogites

4.1.1. Eclogite Facies (M_1)

To estimate the *P-T* conditions of the Dong Co eclogites at different metamorphic stages, *P-T* pseudosections were calculated for the omphacite-bearing samples TC01-1 and TC01-4 using the software THERMOLCALC 3.33 (Figure 7) and the whole-rock composition of TC01-1 and TC01-4 are given in Table 1 and supporting information. In addition, modeled compositional isopleths of garnet (Xprp, Xgrs, and X_{Mg}) have been used to constrain the *P-T* conditions (Figures S1 and S2). The measured compositions of the $Grt_{1\text{-}C}$ and $Grt_{1\text{-}M}$ from sample TC01-1 in equilibrium with omphacites yield conditions of P = ~1.9 GPa, T = ~620°C, and P = 2.4–2.6 GPa, T = ~630°C (Figures S1a and S1b), respectively. The growth zone (core to mantle) of Grt_1

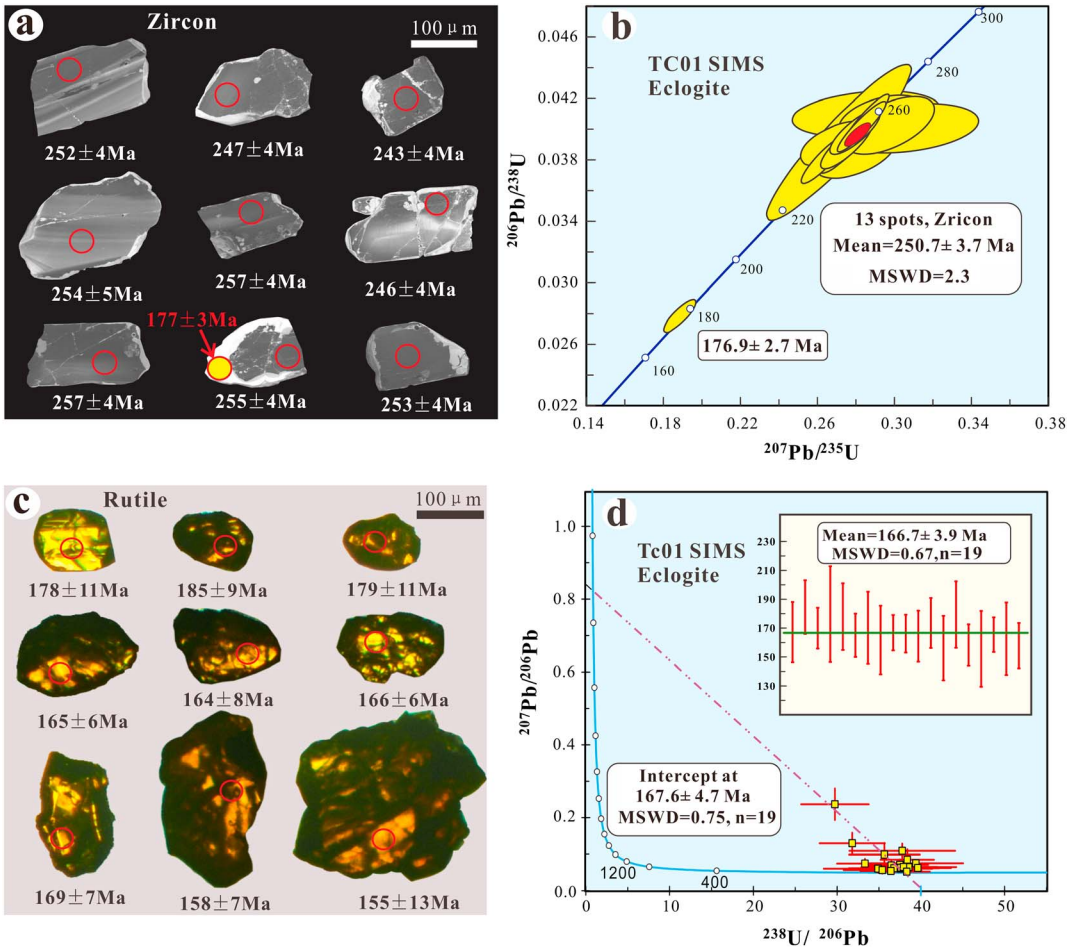

Figure 6. (a) CL images showing the internal structures of the analyzed zircon grains from sample TC01-1; (b) U-Pb concordia diagrams of zircons for sample TC01-1; (c) transmission light images and representative $^{206}Pb^{*}/^{238}U^{*}$ ages of the analyzed rutile grains; (d) U-Pb age concordia diagram for rutiles from sample TC01-1.

defines a near-isothermal compression path from prograde to peak metamorphism which suggests a rapid subduction process. The peak conditions (2.4–2.6 GPa, 610–630°C) estimated from the composition of $Grt_{1\text{-}M}$ of samples TC01-1 and TC01-4 are in the stability field of garnet + omphacite + phengite + rutile + Na-amphibole + lawsonite + quartz (Figures 7, S1b, and S2b). The HP/LT hydrous minerals, lawsonite, Na-amphibole (e.g., glaucophane), and phengite, are highly unstable at high-temperature conditions, and the preservation of these minerals require a rapid exhumation with substantial cooling (e.g., Clarke et al., 2006; Tsujimori et al., 2006; Wei & Clarke, 2011). Hence, the overprinting at HP granulite facies conditions (M_3) may have erased the former HP/LT hydrous mineral relics and only minor micron-sized omphacite + irregular garnet grains have been preserved in some retrograded eclogite samples (TC01-1 and TC01-4).

4.1.2. Early Decompression during Posteclogite Facies (M_2)

The *P-T* conditions of $Cpx_2 + Pl_2$ symplectites after omphacite are difficult to quantitatively constrain because they reflect the attainment of local/domainal equilibrium rather than that of sample-scale equilibrium. Instead, a rough evaluation of reasonable *P-T* range could be inferred by some mineral information and petrographic textures. The compositions of outermost rim of Grt_A, which could be the result of the $Grt_{1\text{-}M}$ being modified by early decompression, define a decompression-dominated trend (i.e., variation of pressure is more significant than that of temperature) (Figures S1c and S2c), suggesting a rapid exhumation process. Based on the textures related to the breakdown of omphacite, this stage of rapid decompression would have lasted until the complete breakdown of omphacite (Omp-out line) (red field in Figures S1a and S2a, P = 1.3–1.5 GPa, T = 720–780°C).

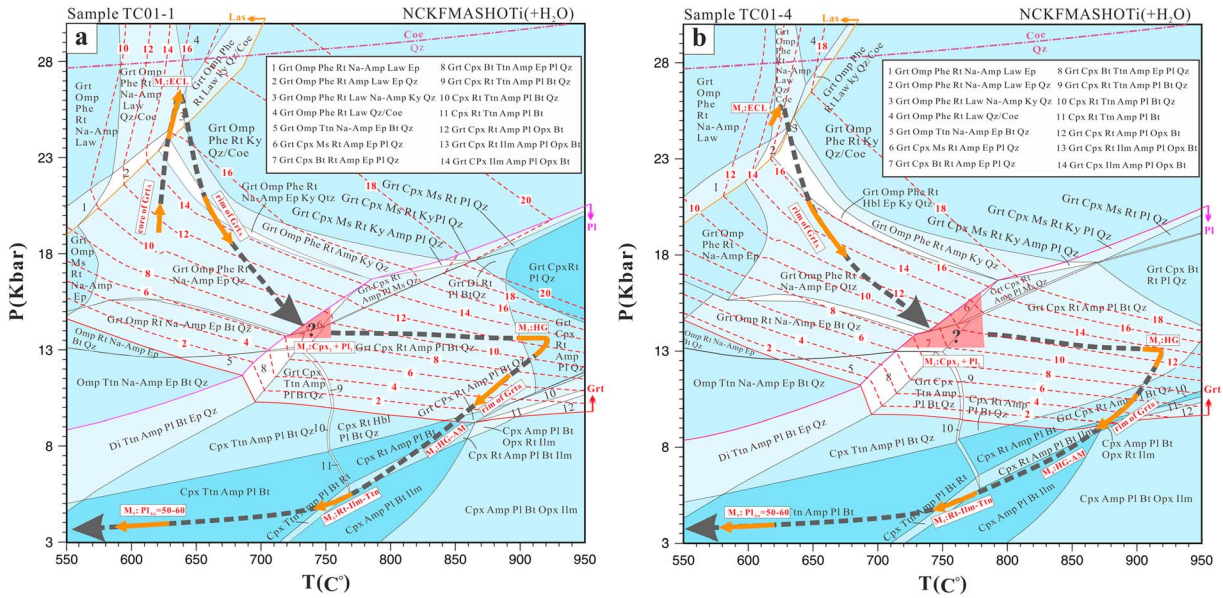

Figure 7. *P-T* pseudosections for the omphacite-bearing samples (a) TC01-1and (b) TC01-4 using the software THERMOLCALC 3.33. Note: The red dashed lines denote the isomodes of garnet (mol %); the orange lines of the *P-T* path are based on the estimates of *P-T* conditions using compositional isopleths of garnet and plagioclase (Figures S1 and S2), while the dashed lines of the *P-T* path indicate conjecture; the red fields denote the conditions at which the Cpx_2 + Pl_2 symplectites were formed in response to the breakdown of the earlier omphacites.

4.1.3. Overprinting of HP Granulite Facies Stage (M_3)

The compositions of Grt_3 yield a *P-T* range of 1.2–1.4 GPa and 910–930°C, which is in the stability field of garnet + clinopyroxene + plagioclase + rutile + amphibole + quartz ± biotite (Figures 7, S1d, and S2d) and nearly in accordance with the actual petrological observations. Biotite was not observed in our investigated samples maybe due to the following reasons: (1) negligible K_2O (0.05–0.16 mol %) in whole-rock composition (Table 1) lead to very low biotite content and (2) the *P-T* conditions of HP granulite facies, just reaching dehydration-melting conditions for biotite (Vielzeuf & Montel, 1994), may have led to the breakdown of the former minor biotite. Although our result (Figure 7) and previous research (e.g., Tsunogae et al., 2003) suggest that some amphiboles (e.g., fluorine-bearing pargasite) can remain stable under the granulite facies conditions (or even higher temperatures), the amphibole grains from M_3 have not yet been identified probably due to their low amount and strong replacement of retrograde amphibole ($Amp_{4–5}$).The *P-T* conditions and mineral assemblage coincide with those of characteristic HP granulite worldwide (Harley, 1989; O'Brien & Rötzler, 2003; X. Z. Zhang et al., 2014), suggesting an overprinting of high temperature metamorphism after the early rapid decompression (M_2).

4.1.4. Late Decompression (M_4) and the Following Amphibolite Facies (M_5) Stages

The M_4 assemblage (Amp_4 + Pl_4 ± Ilm_4 ± Mag_4), as a product of garnet breakdown, is widely developed in symplectites around the Grt_B porphyroblasts, suggesting a rapid decompression process after the HP granulite facies stage (Harley, 1989; O'Brien & Rötzler, 2003; X. Z. Zhang et al., 2014; Zhao et al., 2001). The *P-T* conditions (Figures S1d and S2d) yielded by the compositions of Grt_B rim support a rapid decompression associated with cooling (Figure 7). According to the reaction textures, this decompression *P-T* path would pass through the transition field of rutile-ilmenite-titanite (P = 0.3–0.6 GPa; T = 720–770°C) (Figures S1a and S2a), which grew during the initial stage of amphibolite facies retrograde metamorphism (M_5). Then the rocks would have further cooled down to T = ~600°C, P = ~0.3 GPa, according to the compositions of Pl_5 (the minimum An = 57) (Figures S1a and S2a), which represent the *P-T* conditions of late stage amphibolite facies retrograde metamorphism (M_5).

4.2. Zircon and Rutile U-Pb Age and the Geological Significance

Most zircon grains from the Dong Co eclogites are characterized by broadly spaced zoning texture in CL images and high Th/U ratios, similar to those from gabbro/diabase in ophiolites (e.g., Wang, Wang, Chung,

Table 4
LA-ICP-MS Analyses of Trace Elements in Rutile Grains From the Dong Co Eclogites

	Sc	V	Cr	Ni	Sr	Zr	Nb	Hf	Ta	Pb	Th	U	Nb/Ta	Zr/Hf	$T_{1.0}$	$T_{1.5}$	$T_{2.0}$	$T_{2.5}$	$T_{3.0}$
TC01-01	5.64	1065	676	0.19	1.38	944	774	19.1	31.7	0.04	0.00	0.67	24.4	49.4	751	777	804	831	858
TC01-02	5.68	1164	890	0.11	1.07	1053	875	21.6	35.3	0.03	0.01	0.57	24.8	48.9	761	788	815	842	869
TC01-03	4.78	1371	812	0.23	0.81	1487	541	38.6	28.9	0.13	0.00	1.20	18.7	38.5	796	824	852	880	908
TC01-04	6.41	975	553	0.29	1.08	1146	852	25.2	38.5	0.05	0.00	1.13	22.1	45.5	770	797	824	851	879
TC01-05	5.80	1147	597	0.14	1.14	1135	812	25.2	42.3	0.03	0.00	1.33	19.2	45.1	769	796	823	850	878
TC01-06	5.62	1044	2232	0.10	1.09	1040	587	21.1	20.9	0.02	0.00	1.69	28.1	49.2	760	787	814	841	868
TC01-07	5.12	1020	517	0.34	1.14	1053	1379	22.4	54.7	0.05	0.00	1.80	25.2	47.0	761	788	815	842	869
TC01-09	5.41	1331	811	0.16	0.78	1837	596	47.5	29.4	0.13	0.00	1.22	20.3	38.6	819	848	876	905	933
TC01-09	5.27	1017	303	0.22	1.01	1102	1158	22.3	70.1	0.04	0.00	1.40	16.5	49.5	766	793	820	847	874
TC01-10	6.65	1158	834	0.27	1.27	1032	628	23.9	26.3	0.31	0.00	0.93	23.9	43.1	759	786	813	840	867
TC01-11	4.68	820	793	2.01	1.32	1006	1036	19.7	33.4	2.41	0.02	1.63	31.0	51.1	757	784	811	838	864
TC01-12	5.75	890	491	0.05	1.12	1215	1173	27.7	54.5	0.02	0.00	1.75	21.5	43.9	776	803	830	858	885
TC01-13	5.40	1283	1868	0.22	1.08	959	417	19.7	13.2	0.03	0.00	0.93	31.5	48.6	752	779	806	833	859
TC01-14	4.46	1314	4167	0.13	1.04	984	655	20.3	22.3	0.04	0.00	1.04	29.4	48.4	755	781	808	835	862
TC01-15	4.02	1116	671	0.00	1.18	1236	945	28.5	56.4	0.06	0.00	1.48	16.8	43.4	777	805	832	860	887
TC01-16	5.24	1180	462	0.07	1.07	1055	1029	22.1	70.9	0.08	0.00	1.40	14.5	47.8	761	789	816	843	870
TC01-17	5.17	1010	364	0.06	1.11	1067	1067	22.8	67.5	0.02	0.00	1.80	15.8	46.9	763	790	817	844	871
TC01-18	5.74	1070	505	0.24	1.10	1132	662	24.4	33.2	0.02	0.00	1.44	20.0	46.3	768	796	823	850	877
TC01-19	5.59	1040	496	0.36	1.04	1076	622	22.9	28.8	0.03	0.00	1.61	21.6	47.0	763	791	818	845	872
TC04-1	5.23	1022	433	0.22	1.10	1052	1226	22.4	51.6	0.10	0.00	1.03	23.8	46.9	761	788	815	842	869
TC04-2	4.72	1214	364	0.34	1.13	1203	960	29.1	53.4	0.07	0.00	2.08	18.0	41.3	775	802	829	857	884
TC04-3	7.18	970	498	0.42	1.21	1004	820	20.3	40.3	9.33	0.01	1.17	20.4	49.4	757	784	810	837	864
TC04-4	5.52	1176	484	0.46	1.08	1162	559	27.5	39.9	0.07	0.01	0.34	14.0	42.3	771	798	826	853	880
TC04-5	5.85	988	544	0.19	1.69	979	710	20.6	31.4	0.03	0.44	0.64	22.6	47.5	754	781	808	835	862
TC04-6	5.81	989	612	0.34	1.73	975	585	22.4	36.0	0.07	0.01	0.77	16.2	43.5	754	781	807	834	861
TC04-7	5.50	863	583	0.35	1.02	912	554	19.9	22.7	0.03	0.00	0.77	24.4	45.8	747	774	801	827	854

Note. T1.0, T1.5, T2.0, T2.5, and T3.0 denote the Zr-in-rutile temperatures (°C) at 1.0, 1.5, 2.0, 2.5, and 3.0 GPa, respectively, calculated using the calibration of Tomkins et al. (2007).

et al., 2015; Zhang et al., 2016). Hence, the $^{206}Pb/^{238}U$ ages (mean age = ~250 Ma) obtained from these grains probably represent the time of crystallization for the protolith of the Dong Co eclogites, which is consistent with the results of previous laser ablation-inductively coupled plasma-mass spectrometry (LA-ICP-MS) zircon dating (~252 Ma, Wang, Wang, Xu, et al., 2015; ~260–242 Ma, Zhang et al., 2015). Considering the strong mid-ocean ridge basalts (MORB) affinities of the Dong Co eclogites (Wang, Wang, Xu, et al., 2015), their protolith must have been part of the Late Permian to Early Triassic Bangong-Nujiang Tethys oceanic crust. Meanwhile, the metamorphic rim of one zircon grain yields an Early Jurassic metamorphic age (~177 Ma). Based on available information, we suggest that the metamorphic rim of the zircon grain probably grew during the overprinting process of the HP granulite facies stage (M_3) rather than during the eclogite facies stage (M_1), for the following two reasons: (1) the U-Pb age (~177 Ma) of this metamorphic rim is contemporary with the Early Jurassic HP granulite facies metamorphic event (~179 Ma) in the Amdo area located in the central BNSZ (Xie et al., 2013) and (2) if the metamorphic zircon rim (~177 Ma) would record the eclogite-facies peak event (>80–90 km) and the rutile intercept age (~168 Ma, see below) reflect the timing of amphibolite facies (~15 km), the resulting exhumation rate (>4–5 mm/yr) of Dong Co eclogites would have been even faster than those of "cold eclogites" (e.g., Qiangtang eclogites, Zhai et al., 2011) which experienced a rapid exhumation with substantial cooling. This would be contradictory to the metamorphic evolution (slow exhumation and granulitization) of Dong Co eclogites.

Rutile in the Dong Co eclogites is predicted to be stable from the early HP-UHP eclogite facies (M_1) to the high-pressure granulite facies (M_3) stages (Figure 7). Thus, it is essential to determine at which metamorphic stage the rutile grew. The Zr-in-rutile thermometer (Zack et al., 2004; Watson et al., 2006; Tomkins et al., 2007) provides a good opportunity to establish a direct link between the metamorphic temperature and the history of rutile growth (e.g., Gao et al., 2014; Zheng et al., 2011). The studied rutile has high but variable Zr contents (912–1,800 ppm, Table 4), which are distinctly higher than those of rutile formed at the HP-UHP eclogite facies (<150 ppm) (Chen et al., 2013; Gao et al., 2014; Zheng et al., 2011) but similar to those of rutile

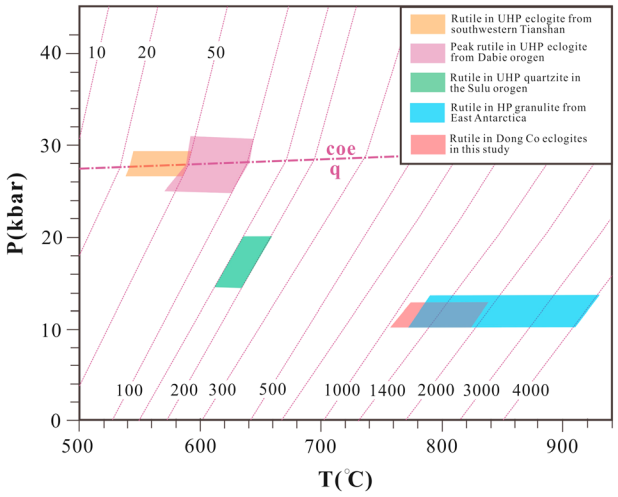

Figure 8. Relationship between Zr isopleths (ppm) and temperature as well as pressure of rutile based on the experimental calibration of Tomkins et al., 2007. Literature data are from Chen et al. (2013), Zheng et al. (2011), Pauly et al. (2016), and Gao et al. (2014).

formed at the granulite facies (Pauly et al., 2016) (Figure 8). Due to the very slow rate of Zr diffusion in rutile (Cherniak et al., 2007), the measured Zr concentrations in rutile could represent the approximate Zr concentrations during the growth process of rutile. The Zr-in-rutile temperatures were calculated using thermometers with pressure-dependent calibration from Tomkins et al. (2007), and the results are listed in Table 4 and Figure 8. Combined with phase equilibrium modeling (Figure 7), the Zr-in-rutile temperatures of 740–850°C calculated at 1.0–1.5 GPa (Table 4) are consistent with the *P-T* evolution of the Dong Co eclogites, suggesting that the rutile was formed during the overprinting process of the HP granulite facies stage. This interpretation is also supported by the mineral occurrence of rutile (Figure 2c).

Interpretation of rutile U-Pb ages is also closely related to the U-Pb closure temperature (T_C), which is dependent on grain size and cooling rate (e.g., Cherniak, 2000; Gao et al., 2014). Experimental studies on lead diffusion suggested T_C of ~600°C and >600°C for rutiles (~100 μm in size) under wet and dry conditions, respectively (Cherniak, 2000). Recently, average T_C of 569 ± 24°C was obtained from rutile grains ranging from 120 to 270 μm (Kooijman et al., 2010). Considering that the analyzed rutile grains mostly range from 150 to 300 μm, the U-Pb T_C for rutile is likely higher, perhaps at about 600°C. The analyzed rutile grains were formed during the HP granulite facies stage with high Zr-in-rutile temperatures (740–850°C), significantly higher than their T_C (~600°C). Therefore, the rutile U-Pb age may reflect the timing when the rocks had cooled from the HP granulite temperature down to ~600°C during the late exhumation process, which should be very close to the timing of the late stage of amphibolite facies retrograde metamorphism (M_5).

In summary, combining the published age of the HP granulite facies metamorphic event (~179 Ma) with our new results from zircon and rutile, we propose that the ~177 Ma zircon age could represent the timing of HP granulite facies overprinting stage, while the rutile lower intercept age of ~168 Ma could reflect the timing of the later stage of amphibolite facies retrograde metamorphism (M_5).

4.3. *P-T-t* Path and Metamorphic Evolution History

The petrographic textures, mineral compositions, and *P-T* pseudosections of the Dong Co eclogites define a complex clockwise *P-T-t* path, including two sections of decompression-dominated *P-T* path (M_1 to M_2 and M_3 to M_4) and one section of heating-dominated *P-T* path (isobaric heating, M_2 to M_3) processes (Figures 7, S1, and S2). Because temperature variations of rocks need prolonged thermal conduction to spread, while pressure variations mainly depend on the depths, decompression-dominated *P-T* paths are generally interpreted as related to rapid exhumation processes after the peak metamorphic conditions (e.g., Harley, 1989; O'Brien & Rötzler, 2003; X. Z. Zhang et al., 2014; Zhao et al., 2001). In contrast, isobaric heating *P-T* paths should reveal a slow exhumation which often resulted in HP granulitic overprinting, similar to what was described for the UHP eclogites from North Qaidam (Song et al., 2003). Therefore, the *P-T-t* path of the Dong Co eclogites reveal a complex metamorphic evolution history in response to a varying rate of the exhumation processes.

Previous research and our new results suggest that the Dong Co eclogites were part of the Late Permian Bangong-Nujiang Tethys oceanic crust which experienced deep subduction (>~80 km) and probably underwent HP-UHP metamorphism (M_1). Because only minor or even trace amounts of early peak metamorphic minerals remain, the timing of the peak metamorphic stage (M_1) is difficult to be determined and it can only be restricted to the period ~250–177 Ma based on our new zircon and rutile U-Pb ages. After the peak metamorphic stage (M_1), the Dong Co eclogites experienced a rapid exhumation process from >80 km to ~50 km, and the symplectites (Cpx_2 + Pl_2) were widely formed in response to the breakdown of omphacite in this stage. In addition, based on isomodes of garnet (mol %) (Figure 7), the garnets from Dong Co eclogites should have experienced a significant decomposition process due to the decrease of modal proportions from M_1 (~15 mol %) to M_2 (~8 mol %) (Figure 7), which is consistent with the observed irregular zoning and corroded appearance of Grt_A (Figures 7, S1, and S2).

Then, the Dong Co eclogites experienced a slow exhumation which resulted in the strong overprinting at HP granulite facies stage (M_3). The U-Pb age of ~177 Ma yielded by the metamorphic rim of one zircon grain should be very close to the timing of the HP granulite facies stage (M_3). Furthermore, the modeled garnet isomodes are also consistent with the observed growth of Mg-rich garnet porphyroblasts during the granulitization process (M_2 to M_3) (Figures 7, S1, and S2). Subsequently, the Dong Co eclogites experienced another rapid exhumation process from ~50 km to ~15 km and underwent amphibolite facies retrogression (M_5), which was restricted to ~168 Ma by the rutile lower intercept age.

5. Geodynamic Implications

Different from the eclogites and blueschists from other typical deeply subducted oceanic crust units (e.g., Zermatt-Saas, Voltri Massif, and Western Himalaya), which generally experienced a simple rapid exhumation (e.g., Agard et al., 2009; Groppo et al., 2016), the Dong Co eclogites are distinguished by the appearance of a slow exhumation period. Although the HP-granulitized eclogites from many other (U)HP terranes have generally been attributed to slow exhumations (O'Brien & Rötzler, 2003; Song et al., 2003), the mechanism is still unresolved. Considering that the closure of the Bangong-Nujiang Tethys Ocean and the continental collision occurred during the Late Jurassic to Early Cretaceous or even later (e.g., Fan et al., 2015; Kapp et al., 2003), the Dong Co eclogites were demonstrably exhumed during oceanic convergence (such as Ecuador of Northern Andes, reviewed by Agard et al., 2009), which need three key steps: (1) eclogite slices/blocks were weakened and detached from the subducting oceanic slab by some mechanism(s) (e.g., Warren, 2013), such as dehydration embrittlement (e.g., Hacker et al., 2003) and/or localized melting (Andersen & Austrheim, 2006; Kanamori et al., 1994); (2) the buoyant material (e.g., serpentinite and sediment) within the subduction channel formed "upward directed channel flow" when their buoyancy exceeded subduction-related traction (Hacker & Gerya, 2013; Warren, 2013); and (3) the detached slices/blocks were carried by the low-viscosity materials flow and exhumed along the subduction channel due to buoyancy (Agard et al., 2009; Guillot et al., 2009; Hacker & Gerya, 2013; Warren, 2013). Because the direction of buoyancy (F_b) is always vertically up, the effective buoyancy (F_e) which drove the eclogites to exhume along the slab should be dependent largely on the dip angle (α) ($F_e = F_b \sin\alpha$). Therefore, the geometry of the slab (flat or steep subduction) would play a key role in the exhumation velocities of a buoyancy-driven exhumation process. Combining regional geological observations with our results, we propose a new flat subduction model in response to the subduction of an overthickened oceanic crust which resulted in the sharp deceleration of exhumation and the overprinting at HP granulite metamorphic conditions.

According to our model, the Bangong-Nujiang Tethys oceanic crust subducted northward beneath the Southern Qiangtang Block at a high/ normal dip angle during the early stage (~250–177 Ma) until the subduction of buoyant overthickened oceanic crust (oceanic plateaus, aseismic ridges, or seamount chains) (Figure 9a). This is strongly supported by the identification of widespread remnants of the Early Jurassic oceanic plateau within the Bangong-Nujiang Tethys Ocean (K. J. Zhang et al., 2014). When arriving at the trench, the overthickened oceanic plateau substantially slowed down the subduction and increased the resistance, triggering the eclogite slices to be detached from the descending eclogitized slab (Figures 9a and 9b). Significant effective buoyancy resulting from a high dip angle drove the eclogite slices/blocks wrapped in low-viscosity materials to return rapidly from a depth of >~80 km to that of ~50 km (Figure 9b). Subsequent subduction of positively buoyant oceanic plateau can lead the slab to dip more shallowly or even horizontally (Figure 9c) based on many numerical models and geophysical studies (e.g., Arrial & Billen, 2013; Gutscher, Spakman, et al., 2000; van Hunen et al., 2002). The very low dip angle can significantly decrease the effective buoyancy along the subducting slab. Therefore, the eclogite slices/blocks are exhumed more slowly or even underplated to the bottom of the overriding plate when they returned into the flat slab segment at a depth of ~50 km (Figures 9c and 9d). Due to the prolonged permanence at the hot crust-mantle transition zone or at the base of thickened lower crust, sufficient thermal conduction heated up the Dong Co eclogites to ~900°C, resulting in their strong overprinting at HP granulite facies conditions at ~177 Ma. Meanwhile, the hypothesis of flat subduction at ~177 Ma is also supported by the simultaneous arc magmatic gaps at the western segments of the BNSZ and the Southern Qiangtang Block (reviewed by Zhu et al., 2013, 2016; Li et al., 2016). As the oceanic plateau was being dragged to depths of ~80–100 km or deeper, negative buoyancy in response to the transition from the oceanic plateau's crust to the eclogites led to a new steep subduction (e.g., Arrial & Billen, 2013). During the process, the Dong Co eclogites experienced another

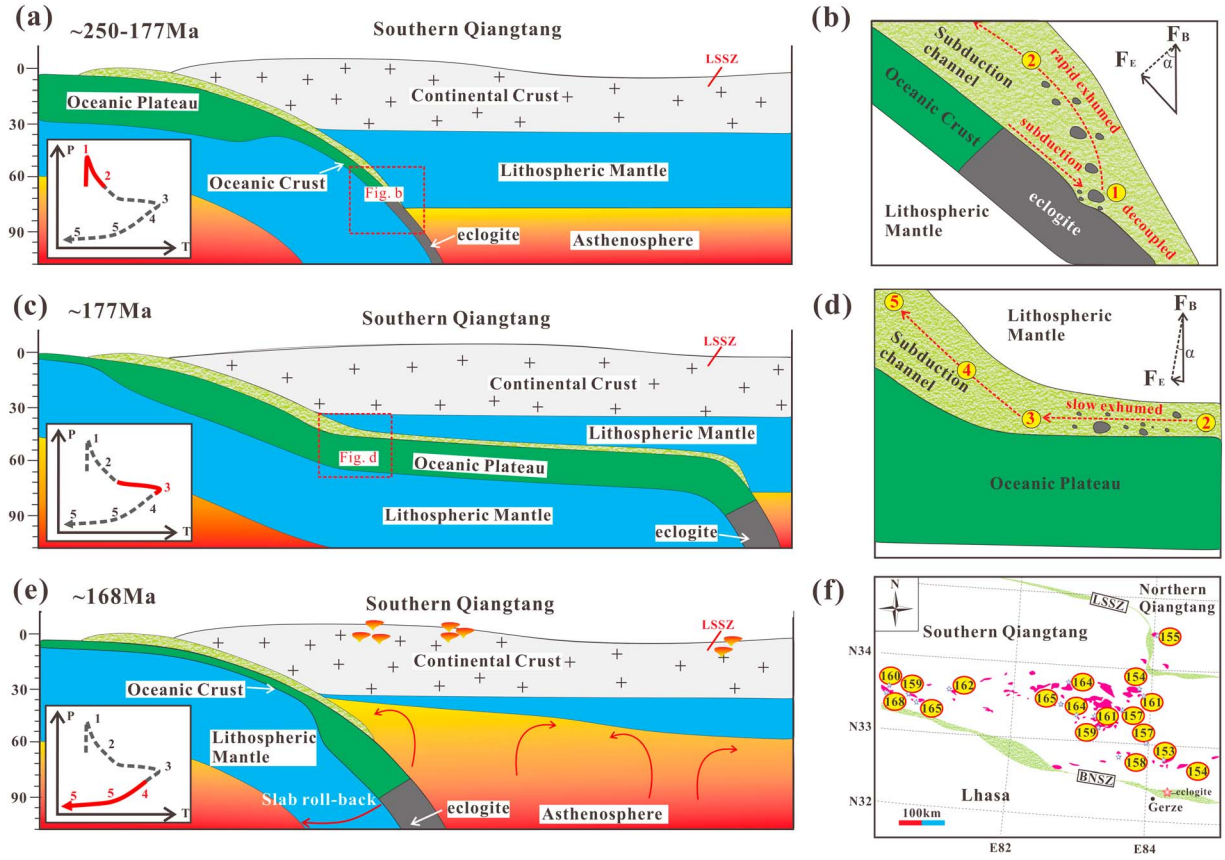

Figure 9. New flat subduction model based on the *P-T-t* path of the Dong Co eclogites for the Bangong-Nujiang Tethys oceanic crust regarding the transition from rapid to slow exhumation and overprinting at HP granulite-facies conditions. (a) Bangong-Nujiang Tethys oceanic crust subducted northward beneath the Southern Qiangtang Block at a high/normal dip angle during the early stage (~250–177 Ma) until the subduction of oceanic plateaus; (b) the overthickened oceanic plateau triggered the eclogite slices to detach from the descending eclogitized slab and the high dip angle led to a rapid exhumation process; (c and d) flat-slab segment made the eclogite slices/blocks difficult to be exhumed and thus were overprinted by HP granulite facies at ~177 Ma; (e) the following slab rollback in response to eclogitization of oceanic plateau resulted in another rapid exhumation process at ~168 Ma; and (f) near-simultaneous or later magmatic rocks formed in response to the slab roll-back (~168 Ma) after the early flat subduction (~177 Ma). The magmatic rocks data are from Li et al. (2016), and references therein. The ~155 Ma granite porphyry data are listed in Figure S3.

rapid exhumation process, returning from ~50 km to ~15 km, and underwent amphibolite facies retrograde metamorphism during the Middle Jurassic (~168 Ma) (Figure 9e). Meanwhile, the asthenosphere upwelling caused by the slab rollback process could have triggered the nearly simultaneous formation of a huge amount of magmatic rocks, which is in agreement with the widespread occurrence of the Middle to Late Jurassic (~168–153 Ma) arc magmatic rocks, adakites, and asthenosphere-derived OIB-type rocks to the north of the BNSZ (Figure 9f) (Li et al., 2016). More importantly, the Middle to Late Jurassic magmatic rocks are not only distributed along the southern margin of the Southern Qiangtang Block, but they have also been found at sites approximately 400 km away from the BNSZ (Figure 9f), further supporting the flat subduction mentioned above.

6. Conclusions

1. The Dong Co eclogites, interpreted as the metamorphic product of the subducted Bangong-Nujiang Tethys oceanic crust, experienced a peak metamorphism at eclogite-facies conditions (T = 610–630°C and P = 2.4–2.6 GPa), strong overprinting at HP granulite facies conditions (T = 910–930°C and P = 1.2–1.4 GPa), and multiple stages of retrograde metamorphism.
2. The Dong Co eclogites experienced a complex clockwise *P-T-t* path, including two sections of decompression-dominated *P-T* path (M_1 to M_2 and M_3 to M_4) and one section of heating-dominated (isobaric heating, M_2 to M_3) processes, which suggests a variation of exhumation velocities.

3. Zircon and rutile SIMS U-Pb dating results suggest that the age of crystallization for the protolith of the Dong Co eclogites is about 250 Ma, that the strong overprinting at HP granulite facies conditions occurred at ~177 Ma, and that the rutile lower intercept age of ~168 Ma could reflect the timing of the late stage of amphibolite facies retrograde metamorphism.
4. Our new results suggest that the slow exhumation in response to flat subduction may have been an important mechanism for the granulite facies overprinting during the exhumation of oceanic eclogites.

Acknowledgments
We sincerely thank Editor-in-Chief Nathan A. Niemi, Associate Editor John Cottle, Chiara Groppo, and an anonymous reviewer for their constructive and insightful reviews. We thank Qiu-Li Li, Xia-Hua Li, Yu Liu, Guo-Qiang Tang, Xiao-Long Huang, and Lin-Li Chen for their assistance in the laboratory operations of rutile SIMS U–Pb dating and EPMA. This study was jointly supported by the National Key R & D Program of China (2016YFC0600407), the Key Program of the Chinese Academy of Sciences (QYZDJ-SSW-DQC026), the National Natural Science Foundation of China (41502054, 41630208, and 41372066), the Talent Project of Guangdong Province (2014TX01Z079), the Guangzhou Institute of Geochemistry, Chinese Academy of Sciences (GIGCAS 135 project (135TP201601)), and the China Postdoctoral Science Foundation funded project (grant 2015M572374). This is contribution IS-2470 from GIGCAS. Additional data sets supporting our conclusions are included in the supporting information files.

References

Agard, P., Yamato, P., Jolivet, L., & Burov, E. (2009). Exhumation of oceanic blueschists and eclogites in subduction zones: Timing and mechanisms. *Earth-Science Reviews*, *92*, 53–79. https://doi.org/10.1016/j.earscirev.2008.11.002

Andersen, T. B., & Austrheim, H. (2006). Fossil earthquakes recorded by pseudotachylites in mantle peridotite from the Alpine subduction complex of Corsica. *Earth and Planetary Science Letters*, *242*, 58–72. https://doi.org/10.1016/j.epsl.2005.11.058

Arrial, P. A., & Billen, M. I. (2013). Influence of geometry and eclogitization on oceanic plateau subduction. *Earth and Planetary Science Letters*, *363*, 34–43. https://doi.org/10.1016/j.epsl.2012.12.011

Bach, W., Erzinger, J., Dosso, L., Bollinger, C., Bougault, H., Etoubleau, J., & Sauerwein, J. (1996). Unusually large Nb-ta depletion in North Chile ridge basalts at 36°50′ to 38°56′S: Major element, trace element and isotopic data. *Earth and Planetary Science Letters*, *142*(1–2), 223–240. https://doi.org/10.1016/0012-821X(96)00095-7

Bach, W., Hegner, E., Erzinger, J., & Satir, M. (1994). Chemical and isotopic variations along the superfast spreading East Pacific Rise from 6 to 30°S. *Contributions to Mineralogy and Petrology*, *116*(4), 365–380. https://doi.org/10.1007/BF00310905

Bézos, A., & Humler, E. (2005). The $Fe^{3+}/\Sigma Fe$ ratios of MORB glasses and their implications for mantle melting. *Geochimica et Cosmochimica Acta*, *69*(3), 711–725. https://doi.org/10.1016/j.gca.2004.07.026

Bourdon, E., Eissen, J., Gutscher, M. A., Hall, M. L., & Cotten, J. (2003). Magmatic response to early aseismic ridge subduction: The Ecuadorian margin case (South America). *Earth and Planetary Science Letters*, *205*(3-4), 123–138. https://doi.org/10.1016/S0012-821X(02)01024-5

Burov, E. B., Jolivet, L., Le Pourhiet, L., & Poliakov, A. (2001). A thermomechanical model of exhumation of HP and UHP methamorphic rocks in Alpine mountain belts. *Tectonophysics*, *342*(1-2), 113–136. https://doi.org/10.1016/S0040-1951(01)00158-5

Byerly, G. (1980). The nature of differentiation trends in some volcanic rocks from the Galapagos spreading center. *Journal of Geophysical Research*, *85*(B7), 3797–3810. https://doi.org/10.1029/JB085iB07p03797

Chen, Z. Y., Zhang, L. F., Du, J. X., & Lü, Z. (2013). Zr-in-rutile thermometry in eclogite and vein from southwestern Tianshan, China. *Journal of Asian Earth Sciences*, *63*, 70–80. https://doi.org/10.1016/j.jseaes.2012.09.033

Cherniak, D. J. (2000). Pb diffusion in rutile. *Contributions to Mineralogy and Petrology*, *139*(2), 198–207. https://doi.org/10.1007/PL00007671

Cherniak, D. J., Mancheste, J., & Watson, E. B. (2007). Zr and Hf diffusion in rutile. *Earth and Planetary Science Letters*, *261*(1-2), 267–279. https://doi.org/10.1016/j.epsl.2007.06.027

Chopin, C. (2003). Ultrahigh-pressure metamorphism: Tracing continental crust into the mantle. *Earth and Planetary Science Letters*, *212*(1-2), 1–14. https://doi.org/10.1016/S0012-821X(03)00261-9

Clarke, G. L., Powell, R., & Fitzherbert, J. A. (2006). The lawsonite paradox: A comparison of field evidence and mineral equilibria modelling. *Journal of Metamorphic Geology*, *24*, 715–725. https://doi.org/10.1111/j.1525-1314.2006.00664.x

Coggon, R., & Holland, T. J. B. (2002). Mixing properties of phengitic micas and revised garnet–phengite thermobarometers. *Journal of Metamorphic Geology*, *20*(7), 683–696. https://doi.org/10.1046/j.1525-1314.2002.00395.x

Cooper, F. J., Platt, J. P., & Anczkiewicz, R. (2011). Constraints on early Franciscan subduction rates from 2–D thermal modeling. *Earth and Planetary Science Letters*, *312*(1-2), 69–79. https://doi.org/10.1016/j.epsl.2011.09.051

Diener, J. F. A., & Powell, R. (2012). Revised activity–composition models for clinopyroxene and amphibole. *Journal of Metamorphic Geology*, *30*(2), 131–142. https://doi.org/10.1111/j.1525-1314.2011.00959.x

Dong, Y. L., Wang, B. D., Zhao, W. X., Yang, T. N., & Xu, J. F. (2016). Discovery of eclogite in the Bangong co–Nujiang ophiolitic mélange, central Tibet, and tectonic implications. *Gondwana Research*, *35*, 115–123. https://doi.org/10.1016/j.gr.2016.03.010

Ellis, S., Beaumont, C., & Pfiffner, O. A. (1999). Geodynamic models of crustal-scale episodic tectonic accretion and underplating in subduction zones. *Journal of Geophysical Research*, *104*(B7), 15169–15190. https://doi.org/10.1029/1999JB900071

Ernst, W. G. (2001). Subduction, ultrahigh-pressure metamorphism, and regurgitation of buoyant crustal slices—Implications for arcs and continental growth. *Physics of the Earth and Planetary Interiors*, *127*(1–4), 253–275. https://doi.org/10.1016/S0031-9201(01)00231-X

Fan, J. J., Li, C., Xie, C. M., Wang, M., & Chen, J. W. (2015). Petrology and U–Pb zircon geochronology of bimodal volcanic rocks from the Maierze Group, northern Tibet: Constraints on the timing of closure of the Banggong–Nujiang Ocean. *Lithos*, *227*, 148–160. https://doi.org/10.1016/j.lithos.2015.03.021

Gao, X. Y., Zheng, Y. F., Xia, X. P., & Chen, Y. X. (2014). U–Pb ages and trace elements of metamorphic rutile from ultrahigh-pressure quartzite in the Sulu orogeny. *Geochimica et Cosmochimica Acta*, *143*, 87–114. https://doi.org/10.1016/j.gca.2014.04.032

Gerya, T. V., Stöckhert, J. M., & Perchuk, A. I. (2002). Exhumation of high-pressure metamorphic rocks in a subduction channel: A numerical simulation. *Tectonics*, *21*(6), 1056. https://doi.org/10.1029/2002TC001406

Groppo, C., Rolfo, F., Liu, Y. C., Deng, L. P., & Wang, A. D. (2015). P-T evolution of elusive UHP eclogites from the Luotian dome (North Dabie zone, china): How far can the thermodynamic modeling lead us? *Lithos*, *226*, 183–200. https://doi.org/10.1016/j.lithos.2014.11.013

Groppo, C., Rolfo, F., Sachan, H. K., & Rai, S. K. (2016). Petrology of blueschist from the western Himalaya (Ladakh, NW India): Exploring the complex behavior of a lawsonite-bearing system in a paleo-accretionary setting. *Lithos*, *252–253*, 41–56.

Guillot, S., Hattori, K., Agard, P., Schwartz, S., & Vidal, O. (2009). *Exhumation processes in oceanic and continental subduction contexts: A review*, (pp. 175–205). Subduction Zone Geodynamics: Springer.

Gutscher, M. A., Maury, R., Eissen, J. P., & Bourdon, E. (2000). Can slab melting be caused by flat subduction? *Geology*, *28*(6), 535–538. https://doi.org/10.1130/0091-7613(2000)28%3C535:CSMBCB%3E2.0.CO;2

Gutscher, M. A., Spakman, W., Bijwaard, H., & Engdahl, E. R. (2000). Geodynamics of flat subduction: Seismicity and tomographic constraints from the Andean margin. *Tectonics*, *19*(5), 814–833. https://doi.org/10.1029/1999TC001152

Hacker, B., Peacock, S., Abers, G. A., & Holloway, S. D. (2003). Subduction factory 2. Are intermediate-depth earthquakes in subducting slabs linked to metamorphic dehydration reactions? *Journal of Geophysical Research*, *108*(B1), 2030. https://doi.org/10.1029/2001JB001129

Hacker, B. R., & Gerya, T. V. (2013). Paradigms, new and old, for ultrahigh-pressure tectonism. *Tectonophysics*, *603*(5), 79–88. https://doi.org/10.1016/j.tecto.2013.05.026

Harley, S. L. (1989). The origins of granulites: A metamorphic perspective. *Geological Magazine*, *126*, 1059–1095.
Holland, T. J. B., & Powell, R. (1998). An internally consistent thermodynamic dataset for phases of petrological interest. *Journal of Metamorphic Geology*, *16*, 309–343.
Holland, T. J. B., & Powell, R. (2003). Activity–composition relations for phases in petrological calculations: An asymmetric multicomponent formulation. *Contributions to Mineralogy and Petrology*, *145*(4), 492–501. https://doi.org/10.1007/s00410-003-0464-z
Huang, X. L., Xu, Y. G., Lo, C. H., Wang, R. C., & Lin, C. Y. (2007). Exsolution lamellae in a clinopyroxene megacryst aggregate from cenozoic basalt, Leizhou peninsula, South China: Petrography and chemical evolution. *Contributions to Mineralogy and Petrology*, *154*(6), 691–705. https://doi.org/10.1007/s00410-007-0218-4
Kanamori, H., Anderson, D. L., & Heaton, T. H. (1994). Frictional melting during the rupture of the 1994 Bolivian earthquake. *Science*, *279*, 839–842.
Kapp, P., Murphy, M. A., Yin, A., Harrison, T. M., Ding, L., & Guo, J. H. (2003). Mesozoic and Cenozoic tectonic evolution of the Shiquanhe area of western Tibet. *Tectonics*, *22*(4), 1029. https://doi.org/10.1029/2001TC001332
Katayama, I., Parkinson, C. D., Okamoto, K., Nakajima, Y., & Maruyama, S. (2000). Supersilicic clinopyroxene and silica exsolution in UHPM eclogite and pelitic gneiss from the Kokchetav massif. Kazakhstan. *American Mineralogist*, *85*(10), 1368–1374. https://doi.org/10.2138/am-2000-1004
Kooijman, E., Mezger, K., & Berndt, J. (2010). Constraints on the U–Pb systematics of metamorphic rutile from in situ LA-ICPMS analysis. *Earth and Planetary Science Letters*, *293*(3-4), 321–330. https://doi.org/10.1016/j.epsl.2010.02.047
Kylander-Clark, A. R. C., Hacker, B. R., Johnson, C. M., Beard, B. L., & Mahlen, N. J. (2009). Slow subduction of a thick ultrahigh-pressure terrane. *Tectonics*, *28*, TC2003. https://doi.org/10.1029/2007TC002251
Leake, B. E., Woolley, A. R., Arps, C. E. S., Birch, W. D., Gilbert, M. C., Grice, J. D., … Guo, Y. Z. (1997). Nomenclature of amphiboles: Report of the subcommittee on amphiboles of the international mineralogical association, commission on new minerals and mineral names. *Canadian Mineralogist*, *35*, 219–246.
Li, Q. L., Lin, W., Su, W., Li, X. H., Shi, Y. H., Liu, Y., & Tang, G. Q. (2011). SIMS U–Pb rutile age of low-temperature eclogites from southwestern Chinese Tianshan, NW China. *Lithos*, *122*(1-2), 76–86. https://doi.org/10.1016/j.lithos.2010.11.007
Li, S. M., Zhu, D. C., Wang, Q., Zhao, Z., Zhang, L. L., Liu, S. A., … Zheng, Y. C. (2016). Slab-derived adakites and subslab asthenosphere-derived OIB-type rocks at 156 ± 2Ma from the north of Gerze, central Tibet: Records of the Bangong–Nujiang oceanic ridge subduction during the Late Jurassic. *Lithos*, *262*, 456–469. https://doi.org/10.1016/j.lithos.2016.07.029
Li, X., Tang, G., Gong, B., Yang, Y., Hou, K., Hu, Z., … Li, W. (2013). Qinghu zircon: A working reference for microbeam analysis of U-Pb age and Hf and O isotopes. *Chinese Science Bulletin*, *58*(36), 4647–4654. https://doi.org/10.1007/s11434-013-5932-x
Li, X. H., Liu, Y., Li, Q. L., Guo, C. H., & Chamberlain, K. R. (2009). Precise determination of Phanerozoic zircon Pb/Pb age by multicollector SIMS without external standardization. *Geochemistry, Geophysics, Geosystems*, *10*, Q04010. https://doi.org/10.1029/2009GC002400
Li, Z. X., & Li, X. H. (2007). Formation of the 1300-km-wide intracontinental orogen and postorogenic magmatic province in Mesozoic South China: A flat-slab subduction model. *Geology*, *35*(2), 179–182. https://doi.org/10.1130/G23193A.1
Liou, J. G., Tsujimori, T., Zhang, R. Y., Katayama, I., & Maruyama, S. (2004). Global UHP metamorphism and continental cubduction/collision: The Himalayan model. *International Geology Review*, *46*(1), 1–27. https://doi.org/10.2747/0020-6814.46.1.1
Liu, Y., Hu, Z., Gao, S., Günther, D., Xu, J., Gao, C., & Chen, H. (2008). In situ analysis of major and trace elements of anhydrous minerals by LA-ICP-MS without applying an internal standard. *Chemical Geology*, *257*(1-2), 34–43. https://doi.org/10.1016/j.chemgeo.2008.08.004
Ludwig, K. R. (2003). User's manual for Isoplot 3.00: A geochronological toolkit for Microsoft Excel: Berkeley CA:, [Kenneth R. Ludwig?].
Möller, C. (1998). Decompressed eclogites in the Sveconorwegian (−Grenvillian) orogen of SW Sweden: Petrology and tectonic implications. *Journal of Metamorphic Geology*, *16*(5), 641–656. https://doi.org/10.1111/j.1525-1314.1998.00160.x
Morimoto, N., Fabries, J., Ferguson, A. K., Ginzburg, I. V., Ross, M., Seifert, F. A., … Gottardi, G. (1988). Nomenclature of pyroxenes. *American Mineralogist*, *73*, 1123–1133.
O'Brien, P. J., & Rötzler, J. (2003). High-pressure granulites: Formation, recovery of peak conditions and implications for tectonics. *Journal of Metamorphic Geology*, *21*(1), 3–20. https://doi.org/10.1046/j.1525-1314.2003.00420.x
Pauly, J., Marschall, H. R., Meyer, H. P., Chatterjee, N., & Monteleone, B. (2016). Prolonged Ediacaran–Cambrian metamorphic history and short-lived high-pressure granulite-facies metamorphism in the H.U. Sverdrupfjella, Dronning Maud Land (East Antarctica): Evidence for continental collision during Gondwana assembly. *Journal of Petrology*, *57*(1), 185–228. https://doi.org/10.1093/petrology/egw005
Powell, R., Holland, T., & Worley, B. (1998). Calculating phase diagrams involving solid solutions via non-linear equations, with examples using THERMOCALC. *Journal of Metamorphic Geology*, *16*(4), 577–588. https://doi.org/10.1111/j.1525-1314.1998.00157.x
Puchelt, H., & Emmermann, R. (1983). Petrogenetic implications of tholeiitic basalt glasses from the East Pacific rise and the Galapagos spreading center. *Chemical Geology*, *38*(1-2), 39–56. https://doi.org/10.1016/0009-2541(83)90044-X
Sláma, J., Košler, J., Condon, D. J., Crowley, J. L., Gerdes, A., Hanchar, J. M., … Whitehouse, M. J. (2008). Plešovice zircon—A new natural reference material for U–Pb and Hf isotopic microanalysis. *Chemical Geology*, *249*(1-2), 1–35. https://doi.org/10.1016/j.chemgeo.2007.11.005
Smyth, J. R. (1980). Cation vacancies and the crystal-chemistry of breakdown reactions in kimberlitic omphacites. *American Mineralogist*, *65*, 1185–1191.
Song, S. G., Yang, J. S., Xu, Z. Q., Liou, J. G., & Shi, R. D. (2003). Metamorphic evolution of the coesite-bearing ultrahigh-pressure terrane in the north Qaidam, northern Tibet, NW China. *Journal of Metamorphic Geology*, *21*(6), 631–644. https://doi.org/10.1046/j.1525-1314.2003.00469.x
Tomkins, H. S., Powell, R., & Ellis, D. J. (2007). The pressure dependence of the zirconium-in-rutile thermometer. *Journal of Metamorphic Geology*, *25*(6), 703–713. https://doi.org/10.1111/j.1525-1314.2007.00724.x
Tsujimori, T., Sisson, V. B., Liou, J. G., Harlow, G. E., & Sorensen, S. S. (2006). Very-low-temperature record of the subduction process: A review of worldwide lawsonite eclogites. *Lithos*, *92*(3-4), 609–624. https://doi.org/10.1016/j.lithos.2006.03.054
Tsunogae, T., Osanai, Y., Owada, M., Toyoshima, T., Hokada, T., & Crowe, W. A. (2003). High fluorine pargasites in ultrahigh temperature granulites from Tonagh Island in the Archean Napier complex, East Antarctica. *Lithos*, *70*(1-2), 21–38. https://doi.org/10.1016/S0024-4937(03)00087-2
van Hunen, J., van den Berg, A. P., & Vlaar, N. J. (2002). The impact of the south-American plate motion and the Nazca Ridge subduction on the flat subduction below South Peru. *Geophysical Research Letters*, *29*(14), 1690. https://doi.org/10.1029/2001GL014004
Vielzeuf, D., & Montel, J. M. (1994). Partial melting of metagreywackes. Part 1. Fluid-absent experiments and phase relationships. *Contributions to Mineralogy and Petrology*, *117*(4), 375–393. https://doi.org/10.1007/BF00307272
Wang, B. D., Wang, L. Q., Chung, S. L., Chen, J. L., Yin, F. G., Liu, H., … Chen, L. K. (2015). Evolution of the Bangong–Nujiang tethyan ocean: Insights from the geochronology and geochemistry of mafic rocks within ophiolites. *Lithos*, *192*, 18–33.

Wang, B. D., Wang, L. Q., Xu, J. F., Chen, L., Zhao, W. X., Peng, T. P., … Li, X. B. (2015). Discovery of high-pressure granulite in Dongcuo area from the western section of Bangong Co–Nujiang suture zone and its tectonic significance [in Chinese with English abstract]. *Geological Bulletin of China*, *34*(9), 1605–1616.

Warren, C. (2013). Exhumation of (ultra-)high-pressure terranes: Concepts and mechanisms. *Solid Earth*, *4*(1), 75–92. https://doi.org/10.5194/se-4-75-2013

Watson, E. B., Wark, D. A., & Thomas, J. B. (2006). Crystallization thermometers for zircon and rutile. *Contributions to Mineralogy and Petrology*, *151*(4), 413–433. https://doi.org/10.1007/s00410-006-0068-5

Wei, C. J., & Clarke, G. L. (2011). Calculated phase equilibria for morb compositions: A reappraisal of the metamorphic evolution of lawsonite eclogites. *Journal of Metamorphic Geology*, *29*(9), 939–952. https://doi.org/10.1111/j.1525-1314.2011.00948.x

White, R. W., Powell, R., & Clarke, G. L. (2002). The interpretation of reaction textures in Ferich metapelitic granulites of the Musgrave Block, central Australia: Constraints from mineral equilibria calculations in the system K_2O–FeO–MgO–Al_2O_3–SiO_2–H_2O–TiO_2–Fe_2O_3. *Journal of Metamorphic Geology*, *20*(1), 41–55. https://doi.org/10.1046/j.0263-4929.2001.00349.x

White, R. W., Powell, R., & Holland, T. J. B. (2007). Progress relating to calculation of partial melting equilibria for metapelites. *Journal of Metamorphic Geology*, *25*(5), 511–527. https://doi.org/10.1111/j.1525-1314.2007.00711.x

White, R. W., Powell, R., Holland, T. J. B., & Worley, B. A. (2000). The effect of TiO_2 and Fe_2O_3 on metapelitic assemblages at greenschist and amphibolite facies conditions: Mineral equilibria calculations in the system K_2O–FeO–MgO–Al_2O_3–SiO_2–H_2O–TiO_2–Fe_2O_3. *Journal of Metamorphic Geology*, *18*(5), 497–511. https://doi.org/10.1046/j.1525-1314.2000.00269.x

Whitehouse, M. J., Claesson, S., Sunde, T., & Vestin, J. (1997). Ion microprobe U-Pb zircon geochronology and correlation of Archaean gneisses from the Lewisian complex of Gruinard Bay, northwestern Scotland. *Geochimica et Cosmochimica Acta*, *61*(20), 4429–4438. https://doi.org/10.1016/S0016-7037(97)00251-2

Whitney, D. L., & Evans, B. W. (2010). Abbreviation for names of rock-forming minerals. *American Mineralogist*, *95*(1), 185–187. https://doi.org/10.2138/am.2010.3371

Williams, I. S. (1998). U–Th–Pb geochronology by ion microprobe. In: McKibben, M.A., Shanks III, W.C., Ridley, W.I. (Eds.), Applications of microanalytical techniques to understanding mineralizing processes, *Reviews in Economic Geology*, *7*, 1–35.

Xie, C. M., Li, C., Su, L., Dong, Y. S., Wu, Y. W., & Xie, Y. W. (2013). Geochronology of high-pressure granulite in the Amdo, Qinghai-Tibet Plateau [in Chinese with English abstract]. *Acta Petrologica Sinica*, *29*(3), 912–922.

Yin, A., & Harrison, T. M. (2000). Geologic evolution of the Himalayan–Tibetan orogeny. *Annual Review of Earth and Planetary Sciences*, *28*(1), 211–280. https://doi.org/10.1146/annurev.earth.28.1.211

Zack, T., Moraes, R., & Kronz, A. (2004). Temperature dependence of Zr in rutile: Empirical calibration of a rutile thermometer. *Contributions to Mineralogy and Petrology*, *148*(4), 471–488. https://doi.org/10.1007/s00410-004-0617-8

Zhai, Q. G., Zhang, R. Y., Jahn, B. M., Li, C., Song, S. G., & Wang, J. (2011). Triassic eclogites from central Qiangtang, northern Tibet, China: Petrology, geochronology and metamorphic P–T path. *Lithos*, *125*(1-2), 173–189. https://doi.org/10.1016/j.lithos.2011.02.004

Zhang, K. J., Xia, B., Zhang, Y. X., Liu, W. L., Zeng, L., Li, J. F., & Xu, L. F. (2014). Central Tibetan Meso-Tethyan oceanic plateau. *Lithos*, *210*, 278–288.

Zhang, X. Z., Dong, Y. S., Li, C., Deng, M. R., Zhang, L., & Xu, W. (2014). Silurian high–pressure granulites from Central Qiangtang, Tibet: Constraints on early Paleozoic collision along the northeastern margin of Gondwana. *Earth and Planetary Science Letters*, *405*, 39–51. https://doi.org/10.1016/j.epsl.2014.08.013

Zhang, X. Z., Dong, Y. S., Wang, Q., Dan, W., Zhang, C., Deng, M. R., … Liang, H. (2016). Carboniferous and Permian evolutionary records for the Paleo-Tethys Ocean constrained by newly discovered Xiangtaohu ophiolites from central Qiangtang, central Tibet. *Tectonics*, *35*(7), 1670–1686. https://doi.org/10.1002/2016TC004170

Zhang, X. Z., Dong, Y. S., Xie, C. M., & Xie, Y. W. (2010). Identification and significance of high-pressure granulite in Anduo area, Tibetan Plateau [in Chinese with English abstract]. *Acta Petrologica Sinica*, *26*(7), 2106–2112.

Zhang, Y. X., Li, Z. W., Zhu, L. D., Zhang, K. J., Yang, W. G., & Jin, X. (2015). Newly discovered eclogites from the Bangong Meso–Tethyan suture zone (Gaize, central Tibet, western China): Mineralogy, geochemistry, geochronology, and tectonic implications. *International Geology Review*, *58*(5), 1–14.

Zhao, G., Cawood, P. A., Wilde, S. A., & Lu, L. (2001). High-pressure granulites (retrograded eclogites) from the Hengshan Complex, North China Craton: Petrology and tectonic implications. *Journal of Petrology*, *42*(6), 1141–1170. https://doi.org/10.1093/petrology/42.6.1141

Zhao, S., Nee, P., Green, H. W., & Dobrzhinetskaya, L. F. (2011). Ca-eskola component in clinopyroxene: Experimental studies at high pressures and high temperatures in multianvil apparatus. *Earth and Planetary Science Letters*, *307*(3-4), 517–524. https://doi.org/10.1016/j.epsl.2011.05.026

Zheng, Y.-F., Gao, X.-Y., Chen, R.-X., & Gao, T. S. (2011). Zr-in-rutile thermometry of eclogite in the Dabie orogen: Constraints on rutile growth during continental subduction-zone metamorphism. *Journal of Asian Earth Sciences*, *40*(2), 427–451. https://doi.org/10.1016/j.jseaes.2010.09.008

Zhu, D. C., Li, S. M., Cawood, P. A., Wang, Q., Zhao, Z. D., Liu, S. A., & Wang, L. Q. (2016). Assembly of the Lhasa and Qiangtang terranes in central Tibet by divergent double subduction. *Lithos*, *245*, 7–17. https://doi.org/10.1016/j.lithos.2015.06.023

Zhu, D. C., Zhao, Z. D., Niu, Y., Dilek, Y., Hou, Z. Q., & Mo, X. X. (2013). The origin and pre-Cenozoic evolution of the Tibetan Plateau. *Gondwana Research*, *23*(4), 1429–1454. https://doi.org/10.1016/j.gr.2012.02.002